UNIVERSITY OF COPENHAGEN

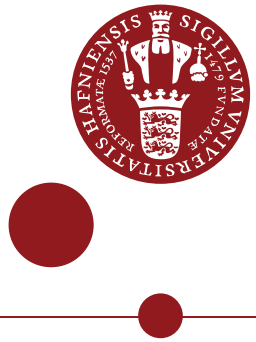

MSc in Astrophysics

The Optical and Infrared Properties of Dusty Star-forming Galaxies in ALCS

Jiaming Yao

Supervised by Prof. Georgios Magdis and Prof. Francesco Maria Valentino

May 2022

Jiaming Yao
The Optical and Infrared Properties of Dusty Star-forming Galaxies in ALCS
MSc in Astrophysics, May 2022
Supervisors: Prof. Georgios Magdis and Prof. Francesco Maria Valentino

University of Copenhagen
Faculty of Science
Cosmic Dawn Center
Jagtvej 128
2200 Copenhagen N

"The most common things in the universe are Hydrogen and Stupidity."

Harland Ellison, 1934

Acknowledgements

This work is my 60 ECTS Master's thesis in astrophysics and was finished at the Cosmic Dawn Center, Niels Bohr Institute, under the instruction of Prof. Francesco Maria Valentino and Prof. Georgios Magdis.

First I would like major thank Prof. Francesco Valentino for guiding me through the whole procedure. Francesco is a prudent, wise, and considerate supervisor. He provides with me suggestions in every aspects, including knowledge and expression of academic results. He is very patient with my dullness and willing to elaborate his points. I also want to thank Prof. Georgios Magdis for providing note as reference for my methods.

Thanks should also go to everyone who has worked and are working in the Master student office of Cosmic Dawn Center. They create a relaxing, friendly, and motivational atmosphere.

Finally, specially thanks to my parents and all other people who are not around me but still encourage me. Their belief in me helps me maintain a positive mind.

Abstract

Dust is a powerful proxy for studying formation of stars and interstellar molecules, and its radiation contributes largely to cosmic infrared background (CIB) which carry information about how early galaxies evolve. The considerable amount of UV radiation produced by these young stars is hidden in the dust around galaxies, thus studying properties of dust can help us reveal a more comprehensive picture of star formation in the early universe. In this thesis, we use photometric catalogues from *ALMA Lensing Cluster Survey* (ALCS) based on the data of the *Hubble Space Telescope* (HST) and *Spitzer*, combining ALMA 1.2mm maps to identify and study properties of dusty star-bursting candidates at $z = 0 \sim 5$. We first directly match sources in optical/NIR catalogues with those in 1.2mm catalogues, then we compare matched objects with color-color diagrams and results of SED fitting to select dusty star-forming candidates. To derive dust mass and total infrared luminosity, we use 1.2mm data to rescale modified black body. Star formation rates are calculated based on UV and infrared luminosity and compared to confirmed relationships in SFR-$M_\star$ plane. The main results are that for galaxies with notable far-infrared radiation, the combination of UV and IR indicators can describe star formation activity of dusty candidates better than SED fitting, and the UVJ diagram can distinguish quiescent galaxies and dusty galaxies with high accuracy.

Contents

1 Introduction

1.1 Galaxy Evolution

After 0.3 Myr from the Big Bang, the cosmic electrons and protons combined and became hydrogen. This procedure, so-called *recombination*, emitted the radiation which people today call cosmic microwave background (CMB), it also created an opaque and dark universe consisting of uniform neutral gas. The dark age lasted for hundreds of millions years until the very first galaxies formed in the dark matter halos and the energy they released ionized the universe. This event is called *reionization*. After the evolution of billions of years, galaxies exhibit different properties in different aspects.

1.1.1 Luminosity Function

A useful tool to characterize the statistical properties of the large universe is the luminosity function. It provides a quantitative description of the number density of galaxies as a function of their luminosity, which has the form of(Schechter, 1976)

$$\frac{dn}{dL} = \phi(L) = \left(\frac{\phi^*}{L^*}\right)\left(\frac{L}{L^*}\right)^{\alpha} e^{-(L/L^*)}, \tag{1.1}$$

where ϕ^* is the normalization density, L^* is the characteristic luminosity above which the number of galaxies declines rapidly, and α is the slope at the faint end, i.e. low luminosity. The luminosity reflects the stellar content or the star formation activities, while the number tells us the statistical information about the universe, e.g. mean luminosity density. Due to the fact that only galaxies that are bright enough can be observed, the luminosity function can be compared to cosmological models and provide constraints on them. Since galaxies formed in different environments can be affected by different mechanisms, it is meaningful only if we consider one specific kind of object when calculating luminosity function, i.e. spiral galaxies or dwarf galaxies. Besides this, luminosities at different bands can reflect different properties, like ultraviolet (UV) luminosity

revealing the distribution of unobscured star formation while information about the dust-obscured star formation is hidden in the infrared luminosity.

1.1.2 Merging

Galaxy mergers are believed to be ubiquitous in the universe. These events can dramatically alter the morphology and luminosity of galaxies. At the late stages of the collision between two galaxies with similar masses, the perturbation of the gravitational field is so large that the stars originally moving in order now would leave their primitive orbits and start random motions, which is called *violent relaxation* (van Albada, 1982). If two spiral galaxies collide, the gas reservoir at their spiral arms is compressed and shocked, resulting in vigorous star formation in a very short time, i.e. a starburst. Galaxies are distorted and stars originally reside in spiral arms are dragged into the central region. The aftermath of this process is normally the elliptical galaxy. When the mass and sizes of two merging galaxies differ enormously, these events are usually called *cannibalism* (Tremaine *et al.*, 1975; Hausman and Ostriker, 1978). In this case, the smaller galaxies will be swallowed by the larger monsters, whose luminosity and mass will not be affected remarkably.

1.1.3 Morphology

The morphology of galaxies is the most direct reflection of the diversity of galaxies. Back in the early 20th century, Edwin Hubble invented the well-known *Hubble sequence*, a morphological classification scheme of galaxies. The two most distinct types in the scheme are elliptical galaxies and spiral galaxies, which are characterized by two major components bulge and disk. Elliptical galaxies have only bulges, containing mainly old stars and barely gas, with various ellipticities defined by

$$E = 10 \times \left(1 - \frac{b}{a}\right), \tag{1.2}$$

where a is the major axis and b is the minor axis. The spiral galaxies consist of both bulges and disks, with stars forming at the spiral arms, so their colors are generally bluer than those of bulges. Disks maintain their structure by rotation, while bulges maintain their equilibrium by the internal motions of stars.

1.2 Main Sequence Galaxies

Observations in the local universe reveal the fact that stellar masses correlate with star formation rate (SFR) tightly(Noeske *et al.*, 2007; Daddi *et al.*, 2007). The relationship can be described by using the power law

$$\Psi = \beta M_{\star}^{\alpha}, \tag{1.3}$$

in which Ψ is the SFR and $M_{\star}$ is the stellar mass. Previous work basically focuses on three aspects of the relation: the slope, the scatter, and the normalization. The slope of the relationship α is ranging between 0.6 and 1.2 (Speagle *et al.*, 2014), while the evolution of the slope can be expected at high-mass range (Whitaker *et al.*, 2014). The reason for this increase has not been well studied, but Abramson *et al.*, 2014 (see also Lee *et al.*, 2015, Schreiber *et al.*, 2015) suggests that the increase of quiescent bulge components can cause the fall of SFR toward high mass end. Compared to the evolution of slope with respect to mass, the slope does not vary remarkably across different redshift (Whitaker *et al.*, 2014). Secondly, This main sequence relationship exhibits an intrinsic scatter of $\sim 0.2 - 0.3$ dex (Whitaker *et al.*, 2012). The last aspect of characterizing star formation sequence is the normalization β, which is found to increase with increasing redshift (Whitaker *et al.*, 2014), from 10 $M_{\odot}/\mathrm{yr}^{-1}$ at $z = 0$ to 100 $M_{\odot}/\mathrm{yr}^{-1}$ at $z = 3$ (Pearson *et al.*, 2018). This phenomenon reflects the overall effect of cosmological gas accretion rates on all mass ranges (Whitaker *et al.*, 2014). This observed relation indicates that star formation histories are regular and smoothly declining on mass-dependent timescales, rather than driven by stochastic events like merger events or starbursts.

1.2.1 Dusty Galaxies

Dust plays important role in the star formation and the cycle of baryonic materials. The dust is commonly believed to form from the ejecta released by supernovae and is composed of metal formed during the evolution of stars with a ratio of 30% $\sim$ 50%. Thus the metallicity is related to the amount of dust. The main compositions of the dust include silicate and carbon grains, as well as polycyclic aromatic hydrocarbons (PAHs) (Draine and Li, 2007). The former grains contribute to the extinction in the UV band while the PAH contributes to variant emission lines at the mid-infrared wavelength. Thus a comprehensive

understanding of dust requires multi-wavelength data.

Hydrogen is the most abundant element in the universe, and the different forms of hydrogen can be tracked by different tracers, however among which the molecular hydrogen (H_2) is hard to directly be observed due to its lack of dipole moment. Since dust is an important refuge for atomic hydrogen to form molecular hydrogen, the content of dust can be a useful proxy for estimating the amount of molecular hydrogen (Charnley *et al.*, 1992).

Apart from acting as a proxy for studying interstellar hydrogen and stellar metallicity, the dust itself plays an important role in star formation and galaxy evolution. Omukai *et al.*, 2005 found that the presence of dust cooling can enhance cloud fragmentation and favor the formation of low-mass stars, therefore altering the shape of initial mass function (IMF). For normal star-forming galaxies, nuclear fusion converts gravitational energy into photospheric radiation and emits strong ultraviolet (UV), which is the direct proxy for studying star formation activities. But for dusty star-forming galaxies (DSFGs), even if they have extremely high star formation rates (SFRs), due to the absorption of UV radiation by the dust, the UV radiation cannot characterize the actual star-forming activities. Thus studying the amount and properties of the dust in galaxies can help us retrieve the actual SFRs.

1.3 Deducing Properties from SED

For those distant galaxies, resolving and studying their morphology and kinematics can be tricky and time-consuming. Measuring their flux at each wavelength and fitting an integrated spectral energy distribution (SED) can quantitatively tell us about the properties of galaxies in an efficient way. Methods of SED fitting can generally be categorized as follows: (1) methods that directly compare data and theoretical models Siebenmorgen and Krügel, 2007; (2) methods that combine templates based on empirical models in (1) and use Bayesian inference ((Carnall *et al.*, 2021)). (3) direct modified blackbody fitting (far-infrared only).

To derive the current stellar properties, there are two things we need to know, or we should say assume, in advance. One of them is the initial mass function (IMF), i.e. how stars are there in the initial state of galaxies. The other one

is star formation history (SFH), which describes how and when galaxies form stars during their lifetimes.

1.3.1 Initial Mass Function

The initial mass of a star may be the most crucial factor affecting how this star will evolve in the future. Thus, knowing how many light and massive stars are in galaxies lays down the guideline for how we model the evolution of galaxies. (Salpeter, 1955) proposed the widely-adopted IMF:$N(M)\mathrm{d}M \propto M^{-\alpha}\mathrm{d}M$, where $\alpha = 2.35$, telling that there are more lighter star in galaxies which also contribute more to the total mass. For the flat distribution with $\alpha = 1$, all galaxies with different mass form uniformly in logarithmic space. Recently Kroupa, 2001 and Chabrier, 2003 proposed that initial galaxies could have fewer low-mass stars. However, the models above come from directly counting stars in the local universe, which means that for the high z case things can become complicated, especially for the low mass star because of cosmological dimming. People refer to numerical models and simulations, like Hennebelle and Chabrier, 2008 and Krumholz *et al.*, 2012.

1.3.2 Star Formation History

Assumptions should also be made about how galaxies form new stars, e.g. do galaxies form new stars rapidly in a relatively short time, or continuously and slowly throughout their lifetime? The methods used for estimating SFH can basically be categorized into non-parametric methods and parametric methods. While the former methods can offer more detail of galaxy evolution but require more constraints and computational resources, parametric methods just assume some analytical forms of SFR(t). The major forms of SFH(t) include simple constant SFH, which describes steady and uniform star formation, and the τ model, where SFR $= e^{-t/\tau}$ (Schmidt, 1959). By selecting the time when star-burst sets in (which changes the form of SFH to SFR$(t) = t^{\beta}e^{-t/\tau}$) and combining them linearly, people can use these models to describe global or current properties like ages, stellar mass, and current SFR with small cost. But when coming to the need of studying the detail of past star formation, non-parametric SFH characterization can be more accurate.

1.3.3 Infrared Spectral Energy Distribution

SED is crucial for exploring properties of the dust, including infrared luminosity $L_{\rm IR}$, grain sizes $T_{\rm dust}$, and dust mass $M_{\rm dust}$, etc. The two major methods are radiative transfer models (for example, (Siebenmorgen and Krügel, 2007)) and direct SED fitting by using modified blackbody models. The former can normally provide more detail about properties of the dust. Unfortunately, unlike the SED fitting at UV and optical wavelength where dozens of bands are available, the fitting of infrared SED suffers from a dearth of far-infrared data due to the limitation of resolution and absorption of atmosphere (thus limited ground-based telescopes) and sometimes only several, even one data point available. Thus it is important to assume values of dust emissivity spectral index β and dust temperature $T_{\rm dust}$ carefully.

1.4 Photometry

Photometry is one of the most useful technique of studying flux and related properties at different wavelengths, especially for those unresolved objects which we can only study "blindly" and quantitatively. Compared to spectroscopy, it has advantages of time-saving and being able to deduce variant properties. In this section we will introduce same basic concepts of photometry and methods used for photometry.

1.4.1 Band and Flux

Imaging is usually carried out at different bands. A band can be characterized by effective temperature $\lambda_{\rm eff}$ and bandwidth $\Delta\lambda$, which includes the smallest wavelength and largest wavelength. Normally the received flux density cannot completely reflect the intrinsic flux density of a source, because response of a CCD varies at different wavelengths, which can be characterized by wavelength-dependent function $T(\lambda)$. Assuming the intrinsic flux density of a source is $F_{\rm int}(\lambda)$, the received flux density of a band can be written as

$$F = \frac{\int_a^b F_{\rm int}(\lambda)T(\lambda){\rm d}\lambda}{\int_a^b T(\lambda){\rm d}\lambda}, \tag{1.4}$$

in which a and b are the lower limit and the upper limit of the band. which represents the central wavelength of a band.

1.5 Photometric System

To collect information of a source in different wavelength, people need to define a set of bands and bandpasses, which is called *photometric system*.An early and commonly used photometric system is the Johnson-Morgan or $UBVRI$ system, which covers NIR to optical wavelength.Information of $UBVRI$ system is listed in 1.1. Another popular system originates from the famous *Sloan Digital Sky Survey* (SDSS) which has similar coverage as $UBVRI$ system. Compared to $UBVRI$ system, it has more narrow bandwidths and advantage of getting rid of sky emission.

Filter	$\lambda_{\rm eff}$(nm)	$\Delta\lambda$(nm)
U	360	50
B	430	72
V	550	86
R	650	133
I	820	150

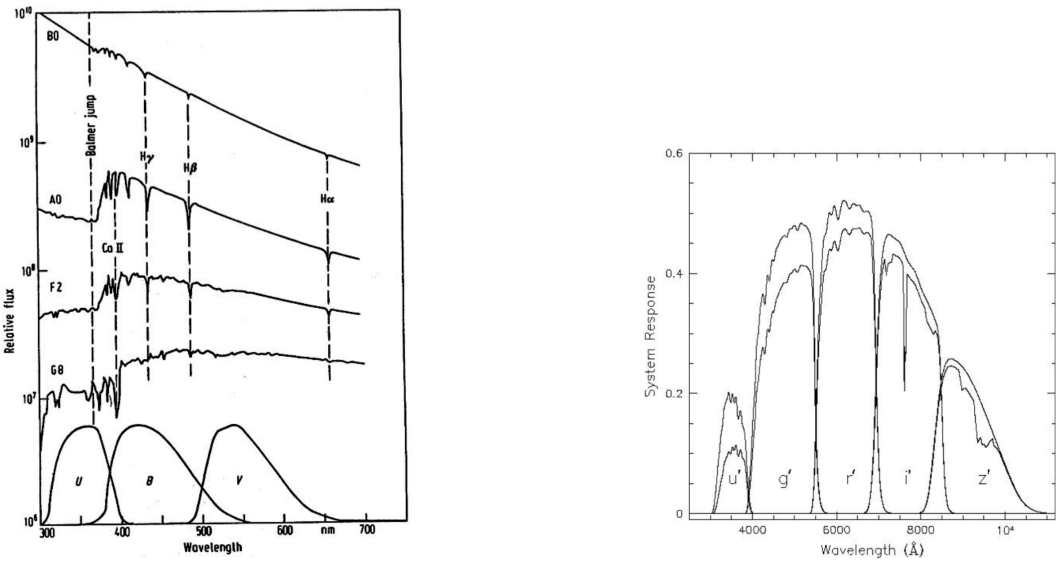

Figure 1.1: *Left*: Coverages of different bands in $UBVRI$ system (Johnson and Morgan, 1953). *Right:* coverages of bands in SDSS system.

1.6 Magnitude System

To express the brightness of celestial objects, astronomers define stellar magnitude as

$$m - m_0 = -2.5\log_{10}\frac{f}{f_0}, \tag{1.5}$$

in which f is the flux density of observed objects, m_0 and f_0 are magnitude and flux density of the reference object, i.e. zero point. This shorthand allows comparing brightness of different sources in a convenient way. For historical reason people choose magnitudes of different bands of Vega as zero points, and magnitudes of every optical bands of Vega are zero. The reason was that Vega was bright enough to be observed, and it had relatively constant magnitudes. But as the observation moves to longer and longer wavelengths and the variation in magnitudes of Vega over years, it turns out that Vega is no more the best choice for calibration. Thus people develop a monochromatic magnitude system, which defines a theoretical zero point for all bands, having the form of

$$m = -2.5\log_{10} f + 8.9 \quad (f \text{ in unit of Jy}) \tag{1.6}$$

This is the AB magnitude system, which we will use in the rest of this thesis. This system helps avoid confusion and inconsistency in astronomical photometry.

1.6.1 Profile-fitting Photometry

The images obtained by telescopes are the convolution of the real images with the point spread function (PSF) of telescopes. PSF basically describes how telescopes respond to a point source. Well-behaved PSFs can generally be described by functions, such as the Gaussian function

$$G(r) \propto \mathrm{e}^{-\left(\frac{r^2}{2a^2}\right)}, \tag{1.7}$$

in which a is the standard deviation, and r is the distance from the center of sources, or a Moffat function (Moffat, 1969):

$$M(r) = \frac{\beta - 1}{\pi\alpha^2}\left(1 + \left(\frac{r}{\alpha}\right)^2\right)^{-\beta}, \tag{1.8}$$

in which $\alpha = \mathrm{FWHM}/(2 \times \sqrt{2^{1/\beta} - 1})$, and $\beta = 4.765$. Normally the Gaussian PSF is a good assumption for the central region of an object, but when coming to the extended wing of it, the Gaussian function is not accurate enough, then we need the Moffat function to get the correct profile. Given the prior shape of PSF, the next step is to match the PSF with the 2-D images and produce the residual map, and maybe repeat the step above iteratively. For a crowded field of sky with many galaxies, multiple PSF-fitting for variant sources can extract information mare accurately. The cost is a large amount of computational resources and time.

1.6.2 Aperture Photometry

Aperture photometry is a method that does not make any assumptions about the shape of the object, but just directly measures all the flux within a defined aperture. The shapes of apertures can be circles, squares, and ellipses. To remove the sky background, one can also define an annulus (in terms of circle aperture), measure median flux in this area, and subtract it from the flux of the object. This procedure can be expressed as

$$F = \mathrm{sum}(A) - \mathrm{median}(B) * npix(A), \tag{1.9}$$

in which A represents the area of the object and B represents the area of the annulus. After background subtraction and estimation of the noise, one can obtain the uncertainty of measured flux.

The advantages of aperture photometry are that it does not require prior knowledge of the shapes of objects so it is computationally cheaper than the fitting method, and aperture photometry can work for those extremely faint objects which people cannot even see them neither can we assume proper functions to fit their profiles. But in contrast to PSF-fitting photometry, aperture photometry cannot be applied in crowded fields well due to severe overlapping of sources, and it does not include the effect of instrument response to the real signal either, which can introduce large error sometimes.

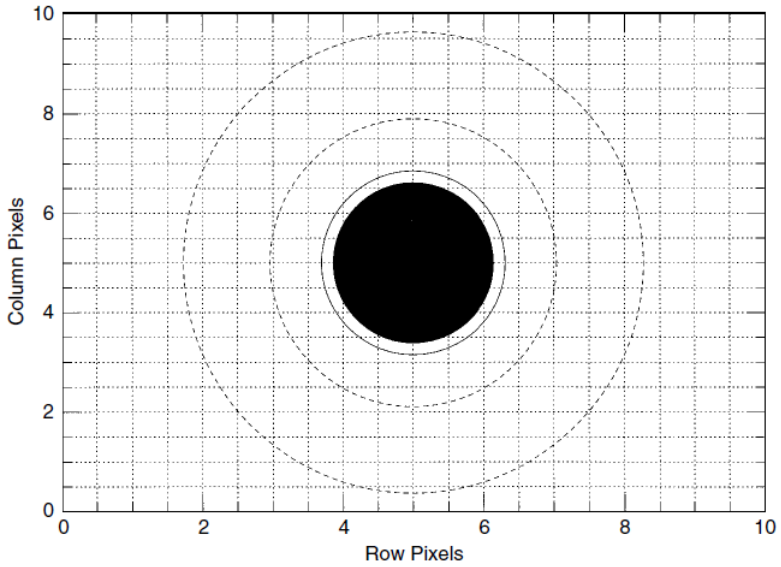

Figure 1.2: Schematic of aperture photometry and noise subtraction (Howell, 2006).

1.7 Goals of This Work

We want to explore the optical properties of ALMA-detected sources in the ALCS survey by exploiting the exquisite ALMA+HST+Spitzer data and the gravitational lensing effect. By selection, we're excluding the dustiest, most star-forming galaxies for which the optical emission is totally absorbed by dust. We want to see what kind of galaxies ALMA picks and if we can reconstruct and push the known trends (main sequence in the $M_\star$ vs SFR relation, $M_{\rm dust}/M_\star$ ratio, optical A_V vs $M_{\rm dust}$, etc.) to lower luminosities or higher redshifts given the gravitational lensing effect.

2 Data

This chapter gives a brief overview of ALCS data used in this thesis, including optical and near-infrared photometry from the *Hubble Space Telescope* (HST) and the *Spitzer Telescope*, as well as far-infrared map from the *Atacama Large Millimeter Array* (ALMA).

2.1 Atacama Large Millimeter Array

The *Atacama Large Millimeter Array* (ALMA) is an interferometric telescope with 66 antennae located on the plateau in the Atacama Desert. It covers wavelengths from 300 μm to 3.6 mm. The long baselines between antennae provide superior resolution with which we can observe and study the weakest signals from cold clouds and dust in the early universe. To make sure these antennae synchronize well with each other, signals are transmitted to the correlator and combined there.

2.2 ALMA Lensing Cluster Survey

The very first galaxies in the universe are ones of the most attractive objects since they carry information from the early universe. Given the large distances between the earth and early galaxies, we cannot directly see the light from those earliest and faintest galaxies with a normal approach. Thanks to the gravitational fields of massive clusters, the light from the distant background galaxies can be magnified and detected by our telescopes. Inspired by this feature, the *ALMA Lensing Cluster Survey* (ALCS, ID:2018.1.00035.L; P.I. Kohno, K.;Kohno, 2019) was proposed to map 88 arcmin^2 sky to a depth of 0.08 mJy, with a duration of 95.5h. The region includes 33 well-studied clusters from the *Cluster Lensing And Supernova Survey with Hubble* (CLASH, Postman *et al.*, 2012), the *Hubble Frontier Fields* (HFF, Lotz *et al.*, 2017), and the *Reionization*

Lensing Cluster Survey (RELICS, Coe *et al.*, 2019). ALCS detected more than 100 sources with S/N >5 (lensing corrected) at 1.15 mm. The catalogue of ALMA 1.15 mm is from Fujimoto et al. (2022, in preparation).

2.2.1 HST and IRAC Data

The ALCS collaboration has recently built photometric catalogues (V. Kokorev, G. Brammer *et al.*, in preparation) which were built by using SExtractor (Bertin and Arnouts, 1996) and *grizli*(Brammer, 2019). The former is a pipeline for image pre-processing and the latter is for background estimation and source detection using aperture photometry mentioned in Section 1.6.2. The parameters of SExtractor for source detection are defined as follow: BACK_FILTTERSIZE = 4arcsec, BACK_FILTER = 3, FILTER = Y, CLEAN = Y, DEBLEND_CONT = 0.001, DEBLEND_NTHRESH = 32, MINAREA = 9, THRESHOLD = 1.0 to maximize the detection of faint objects on the master detection image created from all available ACS/WFC and WFC3/IR filters.
Bands of HST used in our job include F105W, F125W, F127M, F139M, F140W, F153M, F160W, F275WU, F435W, F606W, F814W. Bands of *Spitzer* include IRAC 3.6/4.5 μm.

2.2.2 SED fitting with EAZY

To derive photometric redshift and properties of galaxies, V. Kokorev, G. Brammer *et al.*, (in preparation) use EAZY (Brammer *et al.*, 2008) for SED fitting. EAZY is based on a representative library of SED templates with variant ages, mass-to-light ratios, and SFHs. By comparing observed data points and SED generated from combinations of templates, EAZY finds out the best one with minimized χ^2. After this, the U, V, and J bands used for color-color diagrams, as well as NUV flux, are directly extracted from fixed SEDs.

3 Methods

This section introduces the methods used for matching counterparts of ALMA-detected objects in ALCS catalogs and obtaining their properties.

3.1 Counterpart Matching

To study properties of ALMA-detected objects from UV and infrared wavelengths, we use coordinates of ALCS catalogs and coordinates of ALMA catalogs for matching and only match ALMA-detected sources with S/N>4. We set the threshold of separation as 3 arc seconds.

3.2 UVJ Diagram

The two-colors diagram can be used as a simple tool for probing galaxy evolution. Williams *et al.*, 2009 presented the UVJ diagram which can differentiate quiescent galaxies and star-forming galaxies. The $U-V$ colors sample the Balmer/4000 break. They also illustrated that the border between these two types of galaxies can evolve with time. We adopt definitions of borders from Whitaker *et al.*, 2011. The diagonal selections are expressed as:

$$\begin{aligned}(U-V) &> 0.88\times(V-J)+0.69\ [z<0.5]\\ (U-V) &> 0.88\times(V-J)+0.59\ [z>0.5],\end{aligned} \tag{3.1}$$

while cuts on $U-V$ and $V-J$ are expressed as

$$\begin{aligned}(U-V)>1.3, (V-J)<1.6\ [0.0<z<1.5]\\ (U-V)>1.3, (V-J)<1.5\ [1.5<z<2.0]\\ (U-V)>1.2, (V-J)<1.4\ [2.0<z<3.5],\end{aligned} \tag{3.2}$$

in which U, V, and J are corresponding rest-frame color magnitudes of U, V, and J bands. In terms of the quiescent galaxies and dusty star-bursting galaxies

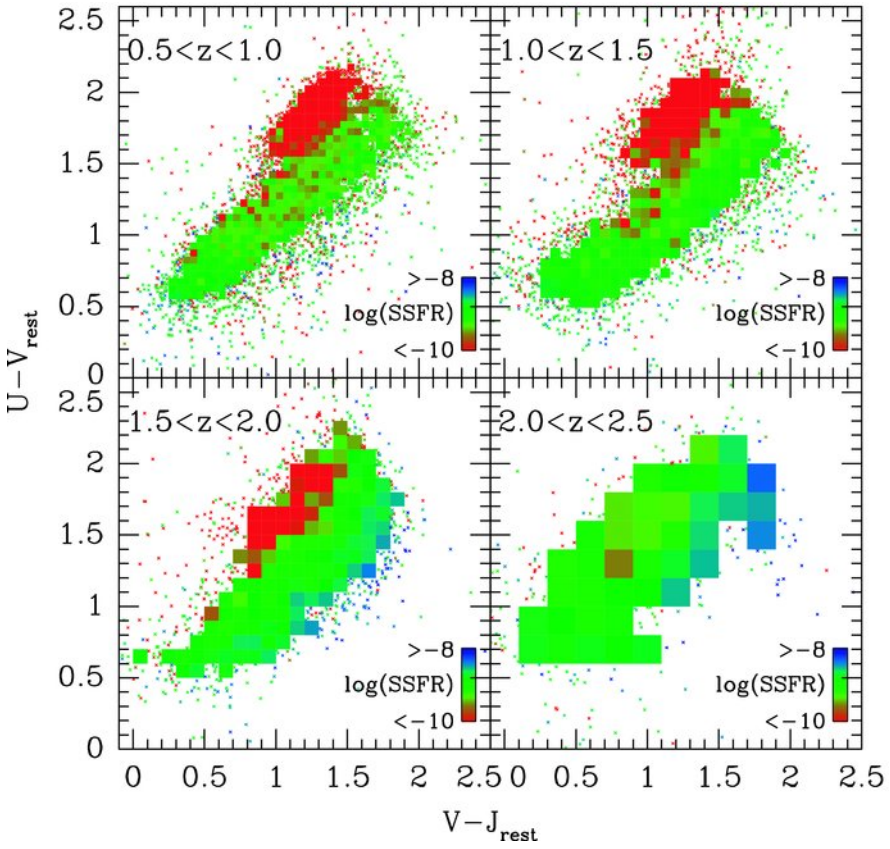

Figure 3.1: Rest frame UVJ diagrams as function of redshift, color-coded by specific star formation rates (sSFR), from Williams *et al.*, 2009. From the figure we can clearly see two types of galaxies populating two distinct regions of maps.

we want to distinguish, they have SEDs with the respective features, as Fig. 3.2 shows. The SED at the left has an excess of near-infrared components compared to the quiescent galaxy, reflecting the existence of a large amount of dust. From their SEDs we have the following relationship:

$$(V-J)_{\text{dusty}} > (V-J)_{\text{quiescent}} \tag{3.3}$$

This difference in the color index can be seen in Fig. 3.3, where dusty star-forming galaxies occupy the upper-right region.

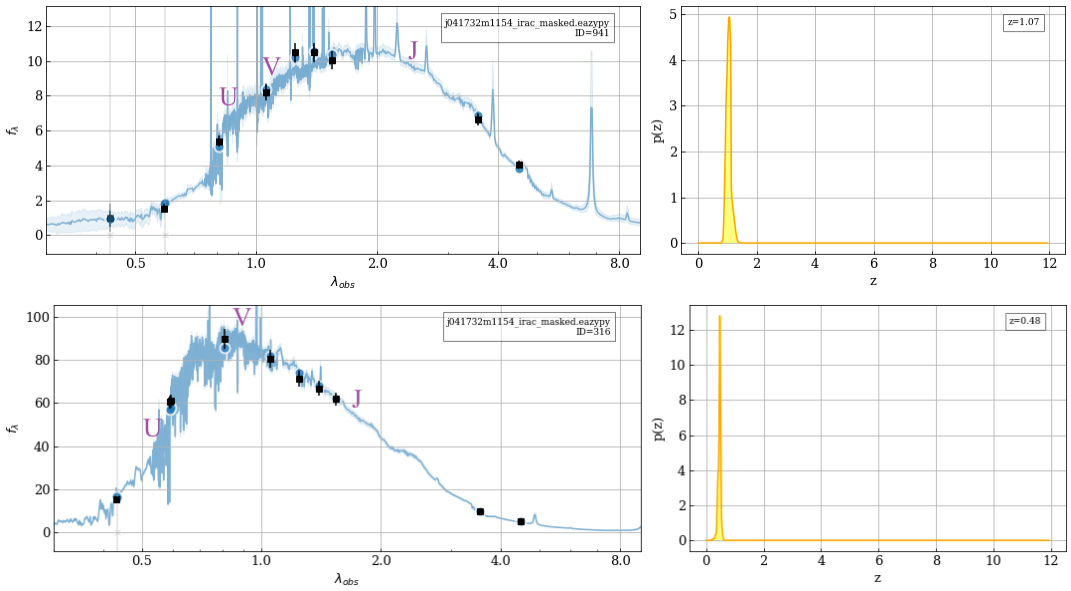

Figure 3.2: *Upper*: SED of a dusty galaxy and probability distribution function(*pdf*) of redshift. *Bottom*: SED of a quiescent galaxy and $pdf(z)$. Based on the inferred redshift from $pdf(z)$ at right, the redshifted wavelengths of rest-frame U, V, and J band are labeled in SEDs.

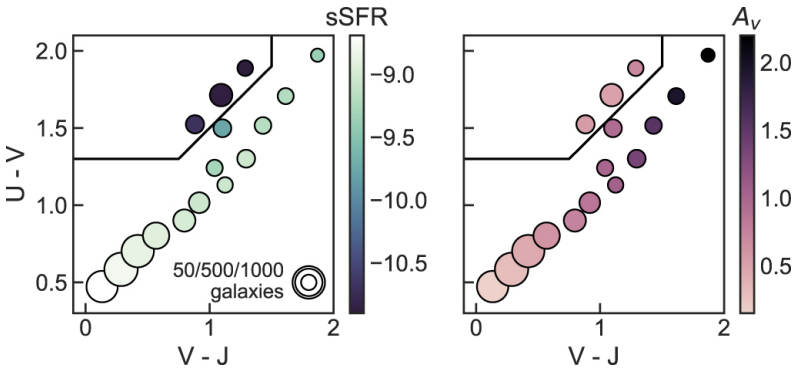

Figure 3.3: UVJ diagrams at $1.0 < z < 2.5$, from Suess *et al.*, 2021. Points are colored by sSFR(*left*) and A_V(*right*). The size of circles is proportional to the number of galaxies at that position. We can see from the left figure that the sSFR decreases slightly when going to the upper-right corner, while it decreases dramatically when entering the quiescent region. A_V increases largely when moving along the track of star-forming galaxies.

3.3 Infrared SED Rescaling

To estimate physical properties from far-infrared data, we use SED modeling to generate infrared SED of dusty candidates. We adopt a Modified Black body curve to carry out rescaling, which can be expressed as

$$S_\nu(T) = \frac{2h}{c^2} \frac{\left(1 - e^{-\tau(\nu)}\right) \nu^3}{e^{h\nu/kT} - 1}, \tag{3.4}$$

in which the optical depth is given by $\tau(\nu) = (\nu/\nu^0)^\beta$. In the optically thin case, the term $1 - e^{\tau(\nu)}$ can be approximated as ν^β, thus the whole MBB becomes

$$S_\nu(T) \propto \frac{\nu^{3+\beta}}{e^{h\nu/kT} - 1}, \tag{3.5}$$

where T is the temperature of the dust in our case, and β is the effective dust emissivity index. Given the only available ALMA data point, we decide to assume a single-T MBB and sample the two parameters of MBB, T and β, from their respective normal distributions. To account for the evolution of dust temperature with respect to the redshift, We adopt the relationship from Schreiber *et al.*, 2018:

$$T_{\rm dust}^{\rm MS}\ [\rm K] = (32.9 \pm 2.4) + (4.60 \pm 0.35) \times (z - 2), \tag{3.6}$$

which describes the evolution dust temperature of main-sequence galaxies, and we assume a normal distribution of β with a peak at 1.8 and a standard deviation of 0.2. Then we sample from these two ranges of parameters 1000 times, inserted them into the MBB, and rescaled the generated SEDs so that they pass through observed data points. For each rescaled SED, we calculate the dust mass by using

$$M_{\rm dust} = \frac{L_\nu}{4\pi\kappa_\nu S_\nu\left(T_{\rm dust}\right)}, \tag{3.7}$$

where L_ν is luminosity at observed $\lambda = 2000\mu$m, κ_ν is the mass absorption coefficient of dust adopting κ_0 of 1.3 cm^2 gr^{-1} at $\lambda_0 = 450\mu$m (Li and Draine, 2001). Also for rescaled SED we calculate the infrared luminosity by integrating the SED from 8 to 1000μm:

$$L_{\rm IR} = \int_{\nu(8\mu m)}^{\nu(1000\mu m)} L_\nu^{\rm MBB} d\nu. \tag{3.8}$$

After the modelling, now we have distributions of SEDs, $M_{\rm dust}$, and $L_{\rm IR}$. We adopt the 50th percentiles of $M_{\rm dust}$ and $L_{\rm IR}$ as representative values, 16th and 84th percentiles as lower and upper bounds of our confidence intervals for every galaxies.

3.4 SFR from UV and Infrared Radiation

The most direct way of obtaining star formation rates (SFRs) is by counting the number of stars of a specific age(Kennicutt and Evans, 2012). However, due to the limitation of instruments, this method can only be applied to the local galaxies. Since those young massive stars will emit strong UV photospheric flux, the UV continuum can directly trace the star-formation activity in the period of 10-200 Myr. But the biggest disadvantage of UV indicator is that it is normally obscured and absorbed by the interstellar medium, like dust, therefore the UV flux cannot directly reflect actual SFR. Luckily if we know the intrinsic color index of the galaxies (Hα/Hβ, for example), it can be used to estimate the dust attenuation and correct for the actual SFR. But the calibration is based on UV luminosity only, which can be negligible in high dust-obscured regions. In this case, the method above may underestimate the SFR. Since the dust absorbs the UV flux and re-emits it in the form of infrared radiation, there is another approach combining UV and infrared luminosity. One of the calibrations we adopt is from Whitaker *et al.*, 2014:

$$\mathrm{SFR}\left[M_{\odot}\mathrm{yr}^{-1}\right] = 1.09\times10^{-10}\left(L_{\rm IR}+2.2L_{\rm UV}\right)\left[L_{\odot}\right], \tag{3.9}$$

where $L_{\rm IR}$ is the total infrared (8-1000μm) luminosity, and $L_{\rm UV}$ is the UV (1216-3000) luminosity. The $L_{\rm UV}$ can be expressed as $L_{\rm UV} = 1.5\nu L_{\nu,280}$

4 Analysis and Results

In this chapter we display our results of analysis and discuss physical processes and possible explanations behind them. $M_\star$, $\mathrm{SFR}_{\mathrm{EAZY}}$, flux density used for SED rescaling, and calculations of SFR are all corrected for magnification.

4.1 Rest-frame UVJ Diagrams

As mentioned in Section 3.2, the UVJ diagram(Williams *et al.*, 2009) can distinguish quiescent galaxies and star-forming galaxies. From these figures we found that the UVJ diagrams exhibit two evolutionary tracks, one is diagonal and it extends from small to large $V-J$ while the other one populates a region with large $U-V$ but small $V-J$. For one $U-V$ value, the dusty star-forming galaxies tend to have larger $V-J$ than quiescent galaxies, as shown in Fig. 3.2. So the diagonal track represents star-forming galaxies with different dust content and the upper-left clump represents quiescent galaxies lacking infrared components. This pattern helps break the degeneracy between *red* quiescent galaxies and *red* star-forming galaxies. We also notice that the young galaxies, known as *blue cloud*, always stand out in the density plots(bottom-left corner) down to $z \sim 0.5$ where dusty star-forming galaxies overtake. This trend agrees well with $\mathrm{SFR}_{\mathrm{EAZY}} - M_\star$ planes discussed in Section 4.2.1, in which most galaxies have mass $< 10^{10} M_\odot$, implying their relatively young ages compared to the typical mass of DFSGs $\sim 10^{11} M_\odot$ (Dye *et al.*, 2008). This phenomenon can be explained by the stellar mass function, which is defined in a similar way as the luminosity function mentioned in Section 1.1.1. For those ALMA-detected objects, we can see that they roughly follow the same diagonal track of star-forming galaxies until $z \sim 0.5$, except for several outliers cross the border and are classified as quiescent galaxies, which we will discuss in the following part. For $0 < z < 0.5$, basically all ALMA-detected sources appear to be either young star-forming galaxies or quiescent galaxies, residing in lensing clusters. Given that the high-density environment in clusters commonly contributes to the quenching of galaxies (Gunn and Gott, 1972; Balogh and Morris, 2000),

plus the low A_V of quiescent galaxies and medium A_V of star-forming galaxies at $0 < z < 0.5$ in Fig. 4.2, these low-redshift ALMA-detected objects are likely mismatched and less dusty galaxies.

4.1.1 UVJ Contamination

Even though UVJ diagram is an efficient and powerful approach to distinguishing quiescent galaxies and star-forming galaxies, it can introduce misclassification for galaxies. By plotting rest-frame UVJ diagrams, we also want to explore how reliable the results from this method are. So we checked SEDs of those ALMA-detected objects that are classified as quiescent. Some of them are very close to the border and thus misclassified partly due to the uncertainty of the UVJ border, some are because of the large error in SED, thus we finally settle down on 2 really misclassified quiescent galaxies out of 20 quiescent galaxies, which SEDs are showed in Fig. 4.3. Just like the typical SED of dusty star-forming galaxies in Fig. 3.2, the existence of dust can be inferred from the notable infrared excess. This small contamination rate($\equiv$ Number of misclassified quiescent galaxies/Total number of detected quiescent galaxies, $\sim 10\%$) proves that the UVJ diagram can distinguish quiescent and dusty galaxies efficiently.

4.2 Main Sequence of ALCS

As mentioned in the Section 1.2.1, a large amount of message about star-formation activities is swallowed by the dust, so that SFR of galaxies possessing vigorous star formation can be underestimated. Thus, by comparing SFRs of these star-bursting galaxies to those of the main sequence, we can see how efficiently dusty candidates can form stars.

4.2.1 $\mathrm{SFR}_{\mathrm{EAZY}} - M_\star$

Figure 4.4 shows SFR $- M_\star$ planes of all HST-detected galaxies. The density plots show all HST-detected objects, while colored points represent ALMA-detected sources. It seems like in every redshift bin the SFR exhibits a tight and clear correlation with stellar mass, having small and uniform dispersion. This could not be considered physical because there should be star-bursting

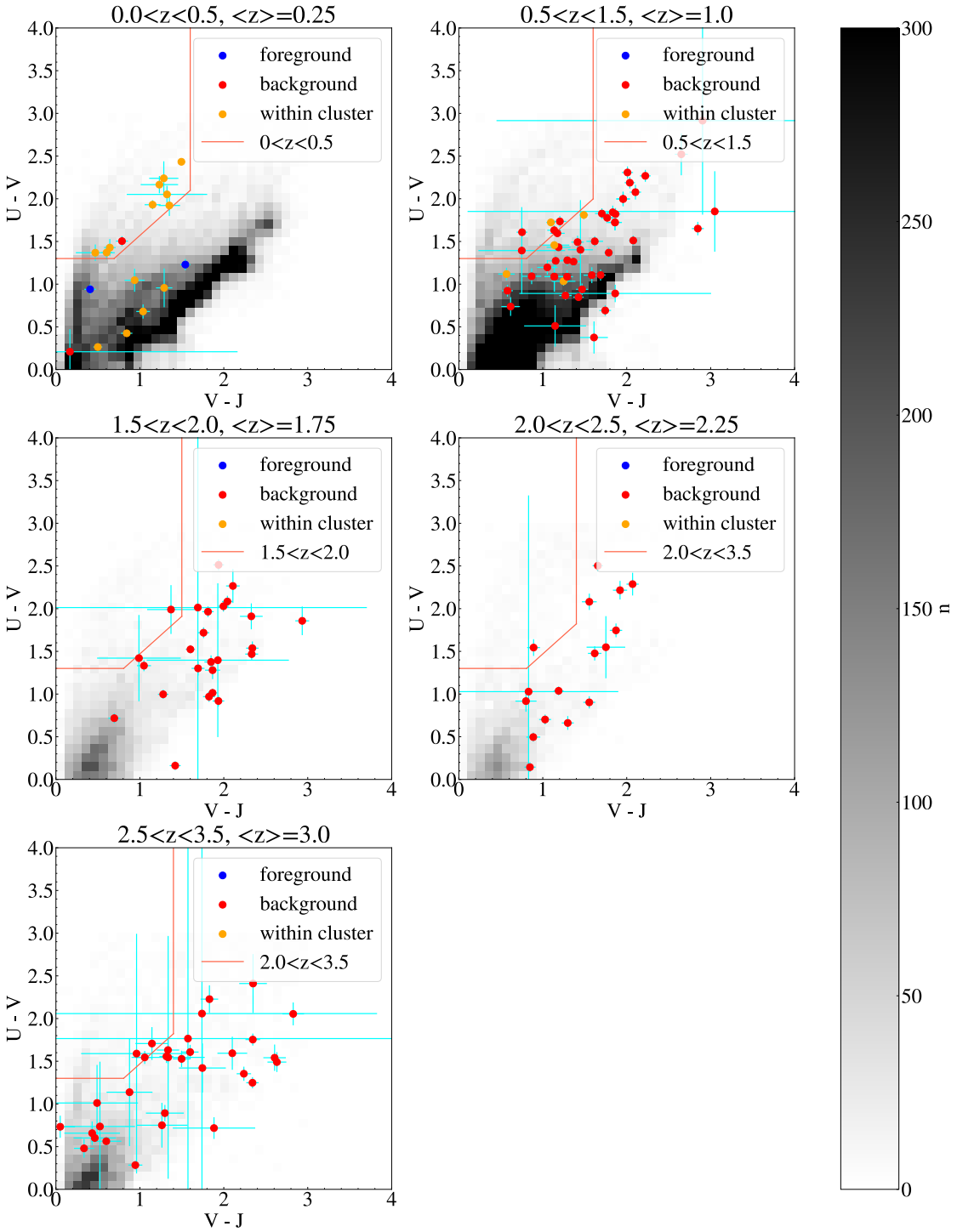

Figure 4.1: *UVJ* diagrams of all galaxies in different redshift bins. The density plots in the background show non-ALMA-detected galaxies and the color represents the number density, while points with different colors show ALMA-detected objects. Red solid lines are from Whitaker *et al.*, 2012. ALMA-detected galaxies are color-coded according to their positions respect to clusters: blue points are galaxies in the foreground, orange points are galaxies within clusters, and red points are galaxies behind the clusters.

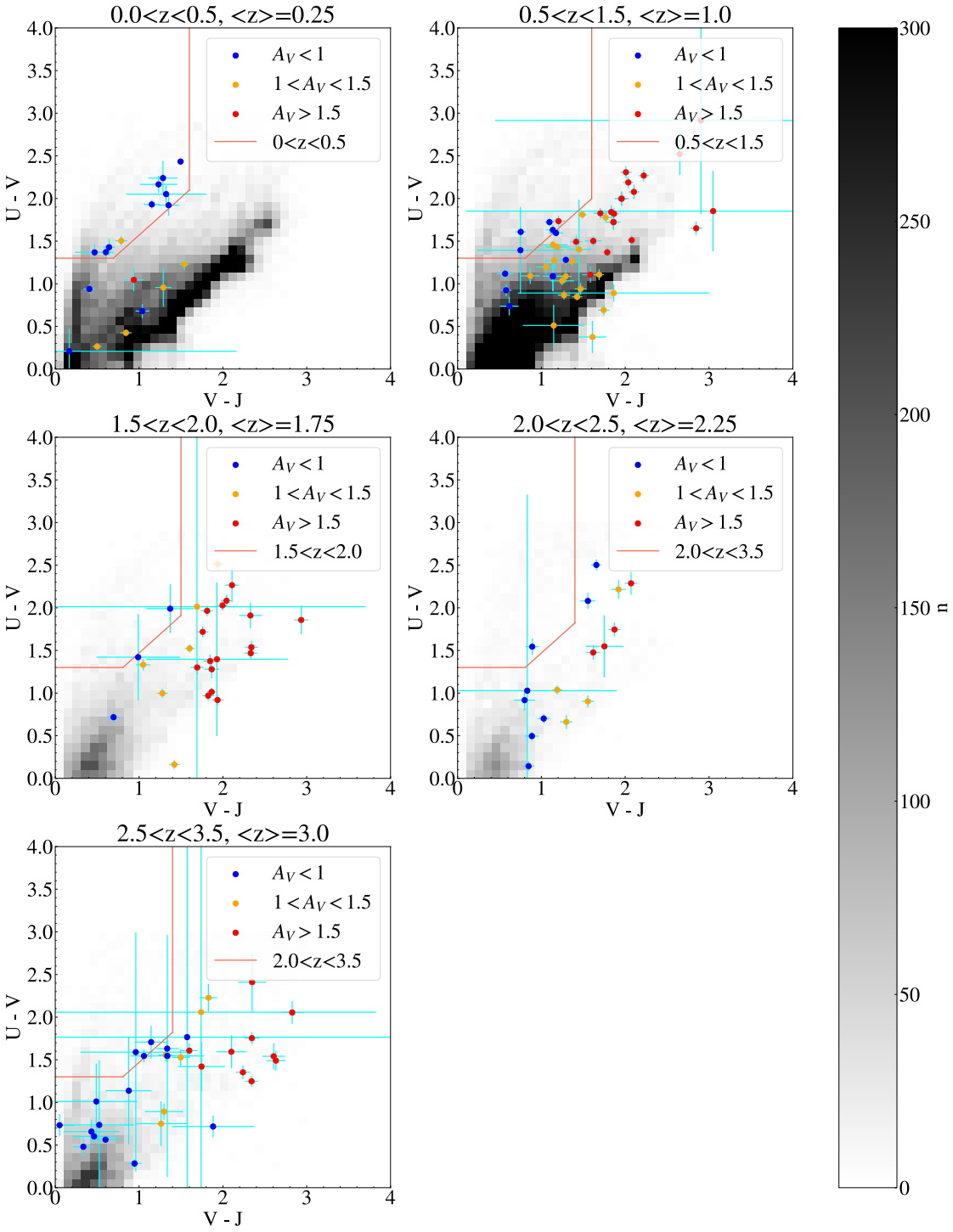

Figure 4.2: UVJ diagrams of all galaxies in different redshift bins. The density plots in the background show non-ALMA-detected galaxies and the color represents the number density, while points with different color show ALMA-detected objects. Red solid lines are from Whitaker *et al.*, 2012. ALMA-detected galaxies are color-coded according to their dust extinction A_V: blue points are galaxies with $A_V < 1$, orange points are galaxies with $1 < A_V < 1.5$, and red points are dusty galaxies with $A_V > 1.5$.

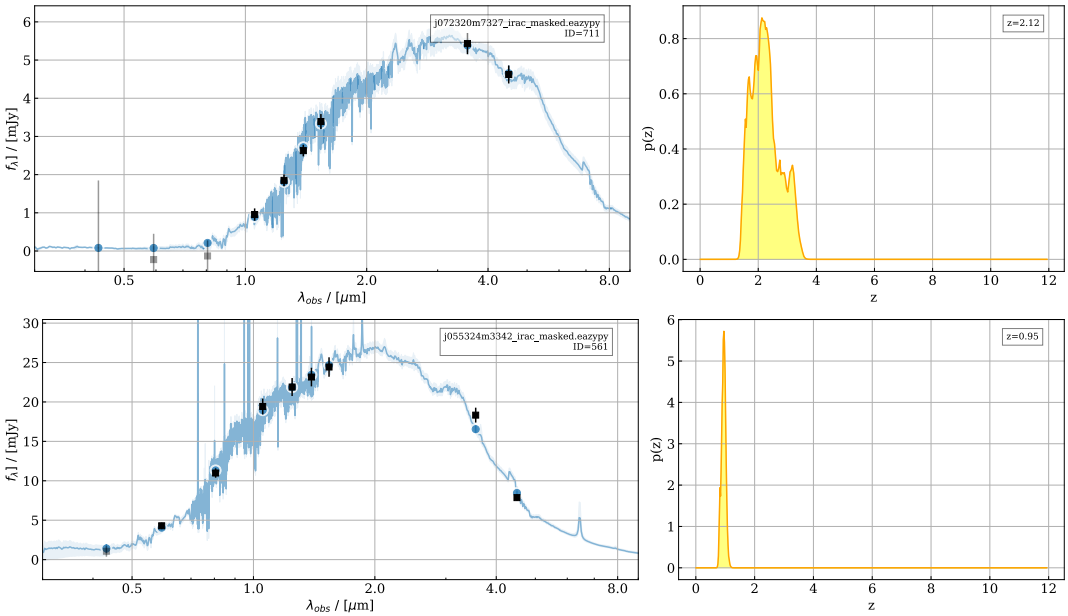

Figure 4.3: SEDs of misclassified quiescent galaxies, *Upper*:SMACSJ0723.3-7327-ID61. *Bottom*: MACSJ0553.4-3342-ID249

galaxies and post-bursting galaxies residing above and under the main sequence. Especially for high-redshift bins, there are only upper bounds (where galaxies are being piled) in density plots, indicating that SFRs of star-bursting galaxies in the early universe are "suppressed" by EAZY, while at $0 < z < 1.5$ lower bounds appear which agrees with the event that galaxies being quenched, but EAZY cannot reflect their low SFRs. The distinct upper and lower bounds of density plots are possibly due to the limits of models in SED fitting. For those ALMA-detected objects, we can also see that most of them have mass $> 10^{10} M_{\odot}$, meaning that they are very likely DSFGs. However they only have SFRs close to or lower than the main sequence, which does not meet our expectation that dusty candidates will experience starburst and exhibit an excess of SFR, thus the SFRs of DSFGs are likely underestimated by EAZY.

4.2.2 $\mathrm{SFR_{EAZY}}$ vs. $\mathrm{SFR_{IR+UV}}$

To investigate how different SFR indicators can affect SFRs with different dust content, we compared SFRs from EAZY ($\mathrm{SFRs_{EAZY}}$) and SFRs calculated from both UV and infrared luminosity ($\mathrm{SFRs_{UV+IR}}$). From Figure 4.5 we can see that a considerable amount of galaxies have elevated $\mathrm{SFRs_{UV+IR}}$ compared to those deduced from SED fitting. We can also see the trend that galaxies with larger elevated $\mathrm{SFR_{UV+IR}}$ tend to have larger $L_{\mathrm{IR}}/L_{\mathrm{UV}}$, and those galaxies with similar

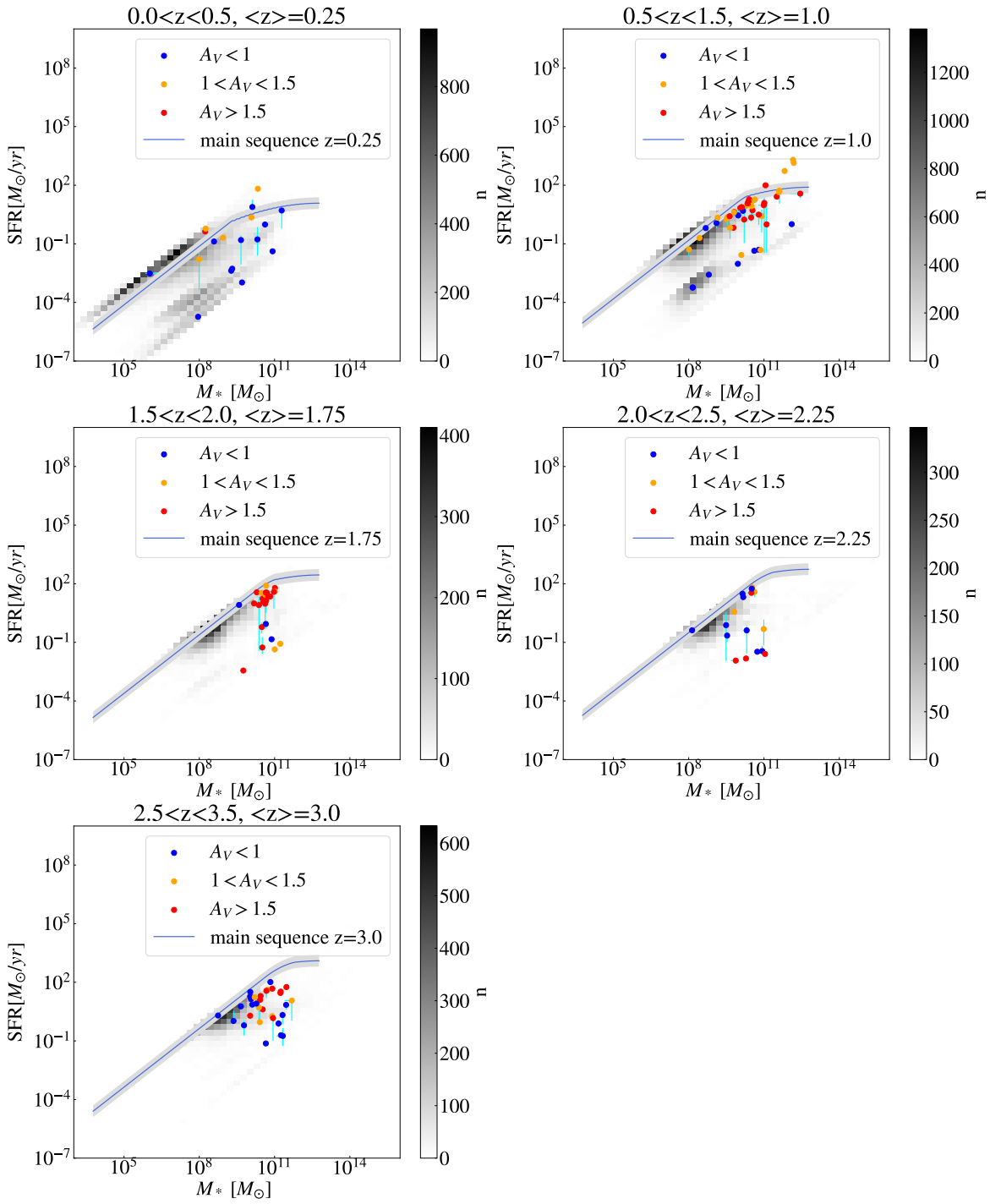

Figure 4.4: $\mathrm{SFR_{EAZY}}$ vs. $M_\star$. The density plots in the background show non-ALMA-detected galaxies and the color represents the number density, while points with different colors show ALMA-detected objects. Blue lines indicate the main sequence of mean redshift in each bin adopted from Schreiber *et al.*, 2015. ALMA-detected galaxies are color-coded according to their dust extinction A_V: blue points are galaxies with $A_V < 1$, orange points are galaxies with $1 < A_V < 1.5$, and red points are dusty galaxies with $A_V > 1.5$.

$\mathrm{SFRs_{EAZY}}$ and $\mathrm{SFRs_{UV+IR}}$ behave the other way. This trend indicates that the reduced UV radiation (that is converted into infrared radiation by dust) can lead to the underestimation of SFR from EAZY, and adding infrared luminosity can alleviate this issue. The assumption of SFH models used in EAZY may lead to the underestimation of SFR, if the starburst event happened far back from now and thus the print of star formation has faded away. On the other hand, assuming a constant SFH can better describe star formation activities in a relatively recent epoch(0 to 100 Myr backward at most, Kennicutt and Evans, 2012), for the conversion we introduce in Section 3.4.

4.2.3 $\mathrm{SFR_{UV+IR}} - M_\star$

To test how well the rescaling of infrared SED can probe hidden star formation, we compare $\mathrm{SFR_{UV+IR}}$ to main-sequence galaxies defined by relationships from Schreiber *et al.*, 2015 for five redshift bins at $0 < z < 5$. When compared with main sequence, DSFGs are often considered to have large *burstiness*, i.e. $\frac{\mathrm{SFR}}{\mathrm{SFR_{MS}}}$. From Fig. 4.6, we can see that combining UV and infrared luminosity can in general lift SFRs of most galaxies up to the level of the main sequence, even above it, compared to $\mathrm{SFR_{EAZY}}$ shown in Fig.4.4. Since all ALMA-detected sources in this work have counterparts in optical/near-infrared data, while those more dusty galaxies might only get dropout and thus be missed, thus our galaxies sample normal star-forming galaxies with small to a large amount of dust, but missing those dustiest star-bursting galaxies, as illustrated in Fig 4.7 (Whitaker *et al.*, 2012). Galaxies at higher z are particularly affected by this selection effect, which can be inferred from the bins of $2 < z < 3.5$ where there are about 1/3 dusty candidates below the main sequence compared to other redshift bins having 1/4 or less, however this need to be validated by more samples. Another trend is that the relatively low redshift galaxies in each bin(except for $0 < z < 0.5$) tend to reside below the sequence. We considered this to be related to our assumption of T_{dust} rising with redshift, and according to Eq. 3.5, the increasing T_{dust} can elevate L_{IR} significantly, thus the $\mathrm{SFR_{UV+IR}}$ more or less is connected with redshift. Besides this, the $T_{\mathrm{dust}}(z)$ we adopt (Eq. 3.6) is derived based on the main sequence galaxies (Schreiber *et al.*, 2018), which means that it likely biases our L_{IR} towards lower values.

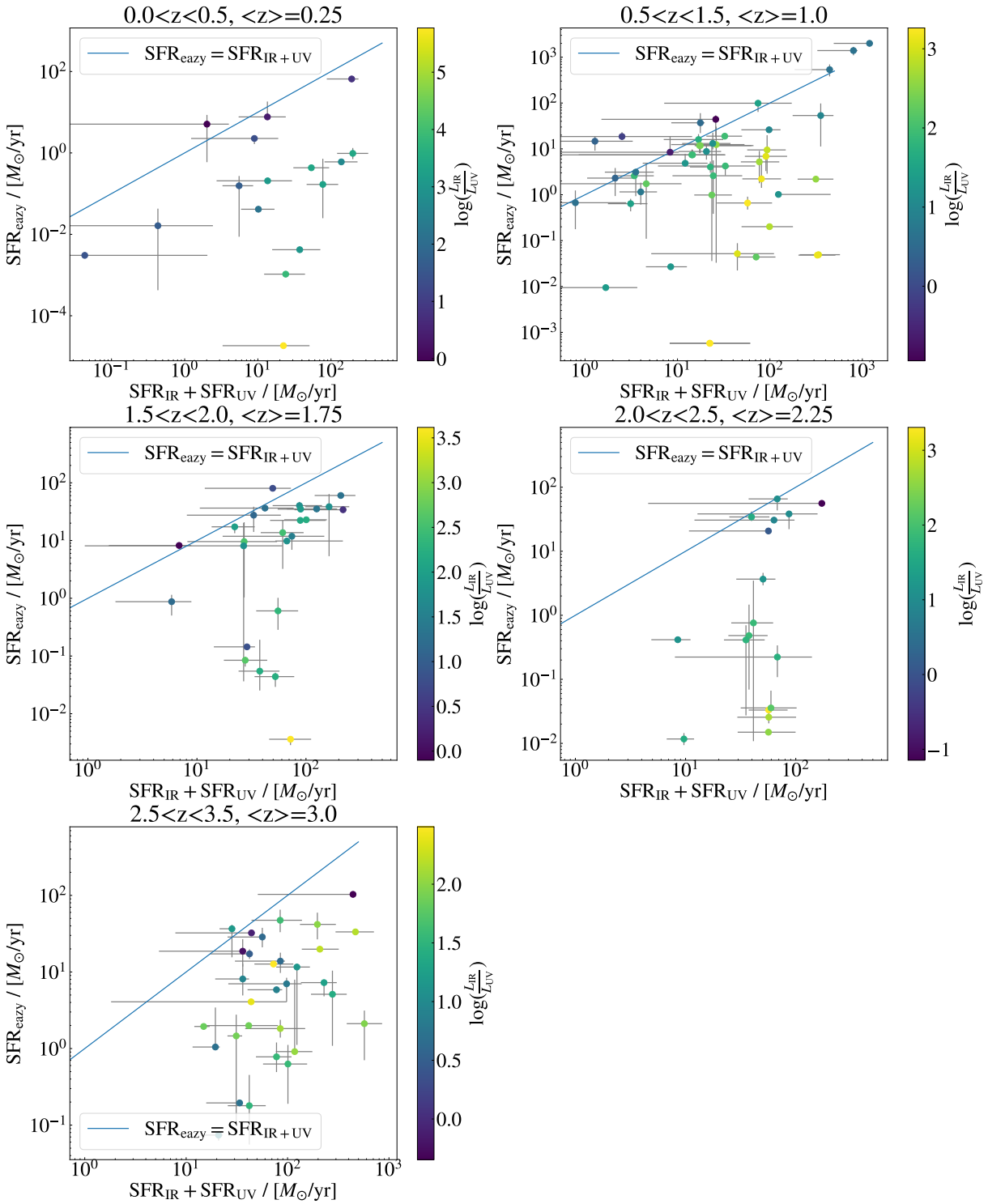

Figure 4.5: SFRs from EAZY vs. SFRs from UV and infrared luminosity, color-coded by $\log \frac{L_{\mathrm{IR}}}{L_{\mathrm{UV}}}$. From these figures we can see that EAZY is likely to underestimate SFRs of galaxies with large dust content which absorb UV radiation and re-emit it in the infrared band.

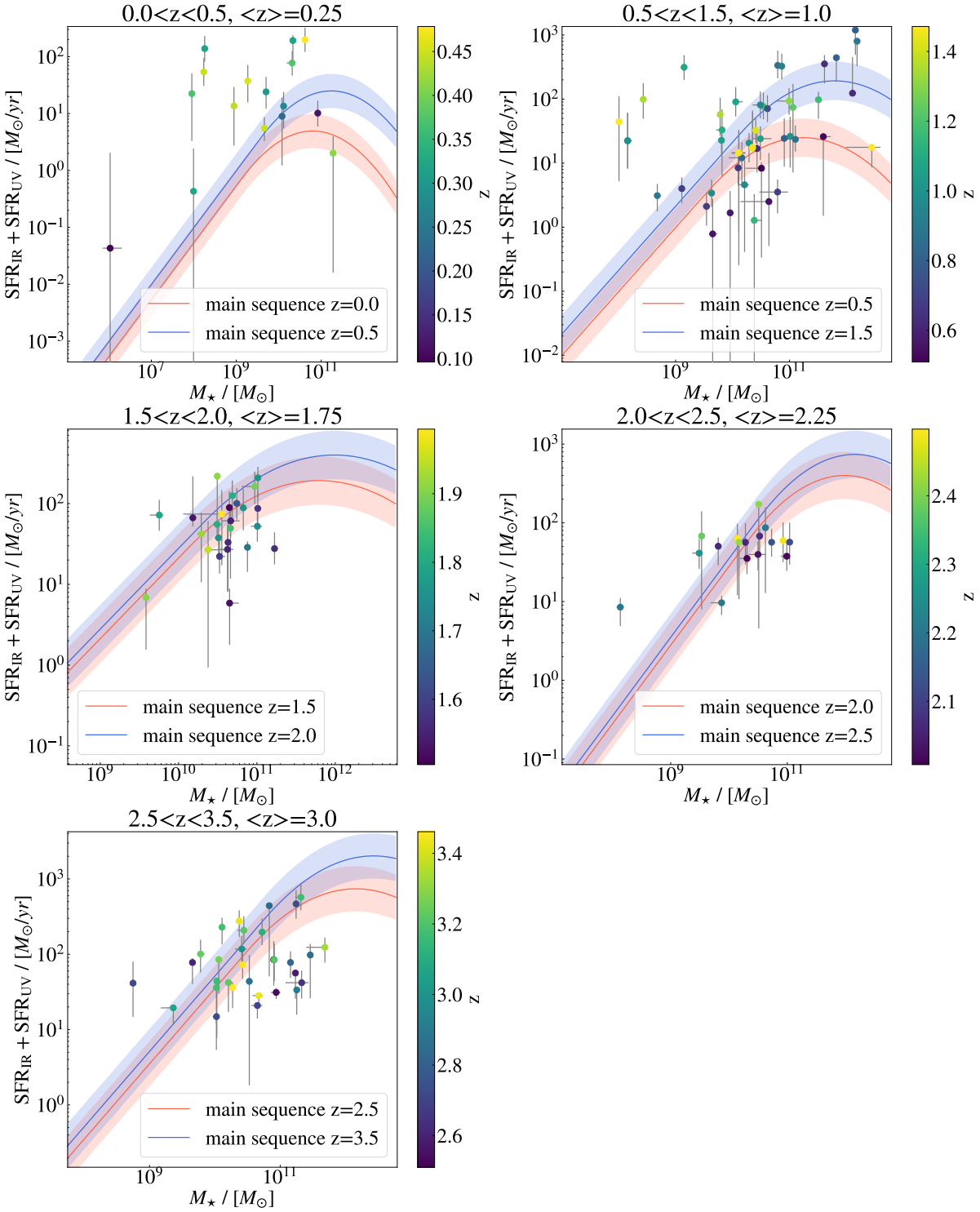

Figure 4.6: M_{stellar} vs. $\text{SFR}_{\text{UV+IR}}$. Objects are color-coded by redshift. The colored lines and corresponding shaded regions are adopted from Schreiber *et al.*, 2015.

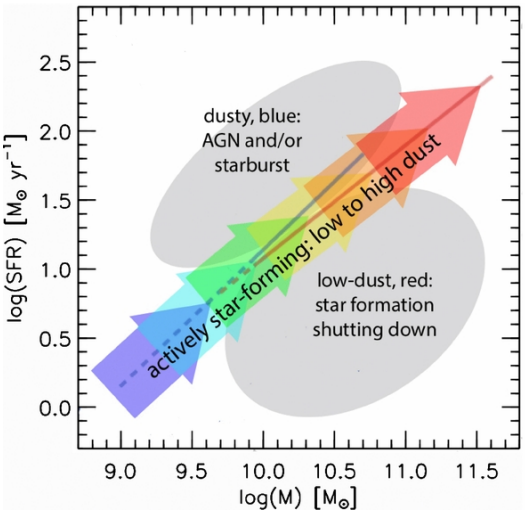

Figure 4.7: Cartoon of how star-forming galaxies with different dust content and SFR populate SFR-$M_\star$ plane from Whitaker *et al.*, 2012. The colorful arrow indicates the evolutionary track of galaxies at the main sequence($\sim 80\%$) with different amounts of dust. A small fraction of extremely dusty galaxies($\sim 7\%$) and dust-free quiescent galaxies reside above and below the main sequence respectively. The rarity of dustiest galaxies can also bias our samples toward normal star-forming galaxies.

4.3 $L_{\rm IR}/L_{\rm UV}-M_\star$

The infrared excess IRX $\equiv \frac{L_{\rm IR}}{L_{\rm UV}}$ probes the amount of star-formation activities hidden behind the dust, and thus the amount of dust in galaxies combined with the tight correlation between IRX and UV continuum slope β (Takeuchi *et al.*, 2012). At first, it is shown in Reddy *et al.*, 2006 that IRX varies as a function of M_*. According to Bouwens *et al.*, 2016, if the dust temperature increases with redshift, then there is little variation of IRX $- M_\star$ up to $z \sim 6$, so we adopt the relationship $\log_{10}$ IRX $= \log_{10}(M_\star) - 9.17$ in Bouwens *et al.*, 2016 as reference for all redshift bins. Like in previous parts, we notice that in Fig. 4.8 there are some outliers with low A_V at $0 < z < 0.5$ having large IRX. This is probably due to ALMA sources mismatched with quiescent galaxies and their low $L_{\rm UV}$ lead to the skyrocketing. At $1.5 < z < 3.5$, we can see that galaxies with $A_V > 1.5$ roughly follow the relationship, except for some outliers. By checking their IDs and comparing them with Figure 4.2, we found that most of these outliers either have large errors in $U - V$ and $V - J$ (which means large errors in SEDs, thus possibly large errors of A_V), or appear as unobscured galaxies in UVJ.

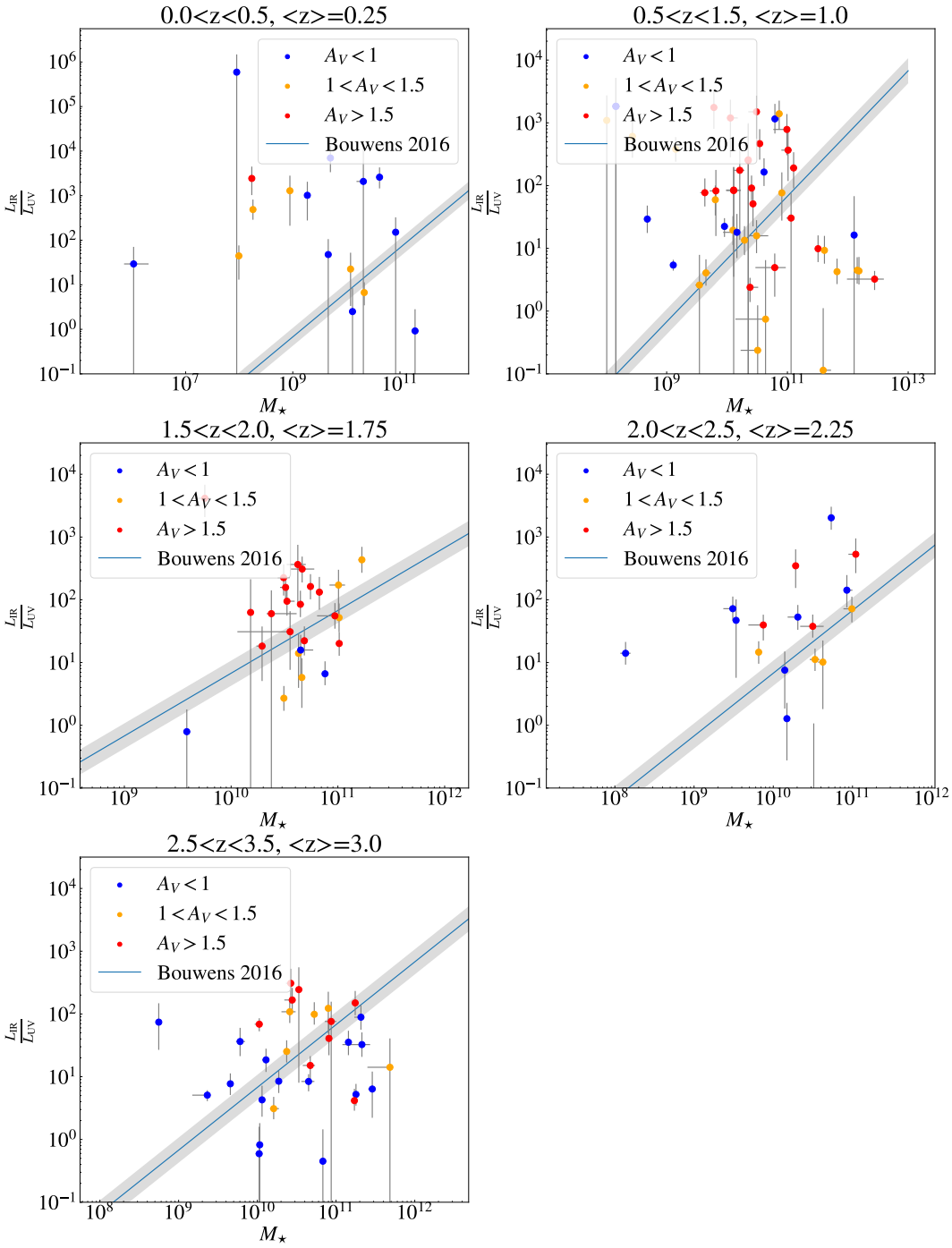

Figure 4.8: $L_{\rm IR}/L_{\rm UV}$ vs. $M_\star$, color-coded by A_V. The blue line represents the relationship adopted from Bouwens *et al.*, 2016.

4.4 Evolution of $M_{\rm dust}/M_\star$

We also test different characterizations of dust. First we explore the relationship between A_V and $M_{\rm dust}$. As Fig. 4.9 shows, we cannot see any clear trend in each redshift bin. We also explore the evolution of $M_{\rm dust}/M_\star$ with respect to $M_\star$, as shown in Fig. 4.10. We found anti-correlation between $M_{\rm dust}/M_\star$ in all redshift bins, which can be the evidence of the dust cycle in galaxies: $M_\star$ evolves with time, while the dust mass declines due to the destruction by shock or radiation from supernovae(Schneider *et al.*, 2004; Silvia *et al.*, 2010), or merging into the stellar mass(Donevski *et al.*, 2020).

We adopt the fitted relationship between $M_{\rm gas}/M_\star$ and $M_\star$ from Magdis *et al.*, 2012 as the main sequence ratio, assuming $M_{\rm gas}/M_{\rm dust} \approx 100$. From Figures 4.10 we can see that except for samples at $0 < z < 0.5$, the evolution of $M_{\rm dust}/M_\star$ in all redshift bins has a similar slope as the reference relationship from Magdis *et al.*, 2012. The median values of $M_{\rm dust}/M_\star$ are displayed at the upper-right corners, which agree well with the range $0.001 \sim 0.01$ of main-sequence galaxies (Béthermin *et al.*, 2015). At redshift $0.5 < 2.5$, $M_{\rm dust}/M_\star$ of our samples, in general, agree well with, even exceed the main sequence ratio, while at higher redshift some galaxies start to fall below the main sequence ratio. Theoretically, the dust mass will be better constrained if the data point is closer to the Rayleigh-Jeans tail (thus better for galaxies at low redshift, see Section 3.3), but according to the result of Schreiber *et al.*, 2018, the monochromatic 1.2 mm measurement of $M_{\rm dust}$ can obtain results with error better than 0.2 dex regardless of redshift. Thus we consider this partly be the consequence of our selection, as mentioned in 4.2.3, that we include ALMA sources only with optical counterparts, which means that only galaxies having a limited amount of dust and sufficient amount of optical radiation can be selected in our samples. Thus our samples are biased towards those less dusty galaxies, especially at higher redshift, as mentioned in Section 4.2.3. Another explanation is that as mentioned in Section 3.3, we adopt the single MBB curve and flux density at the Rayleigh-Jeans tail to probe the dust mass, which assumes single dust temperature and only represents the colder component of the stellar dust (Casey *et al.*, 2014). For those galaxies with hierarchical dust and temperature distribution, this assumption can underestimate the total dust mass.

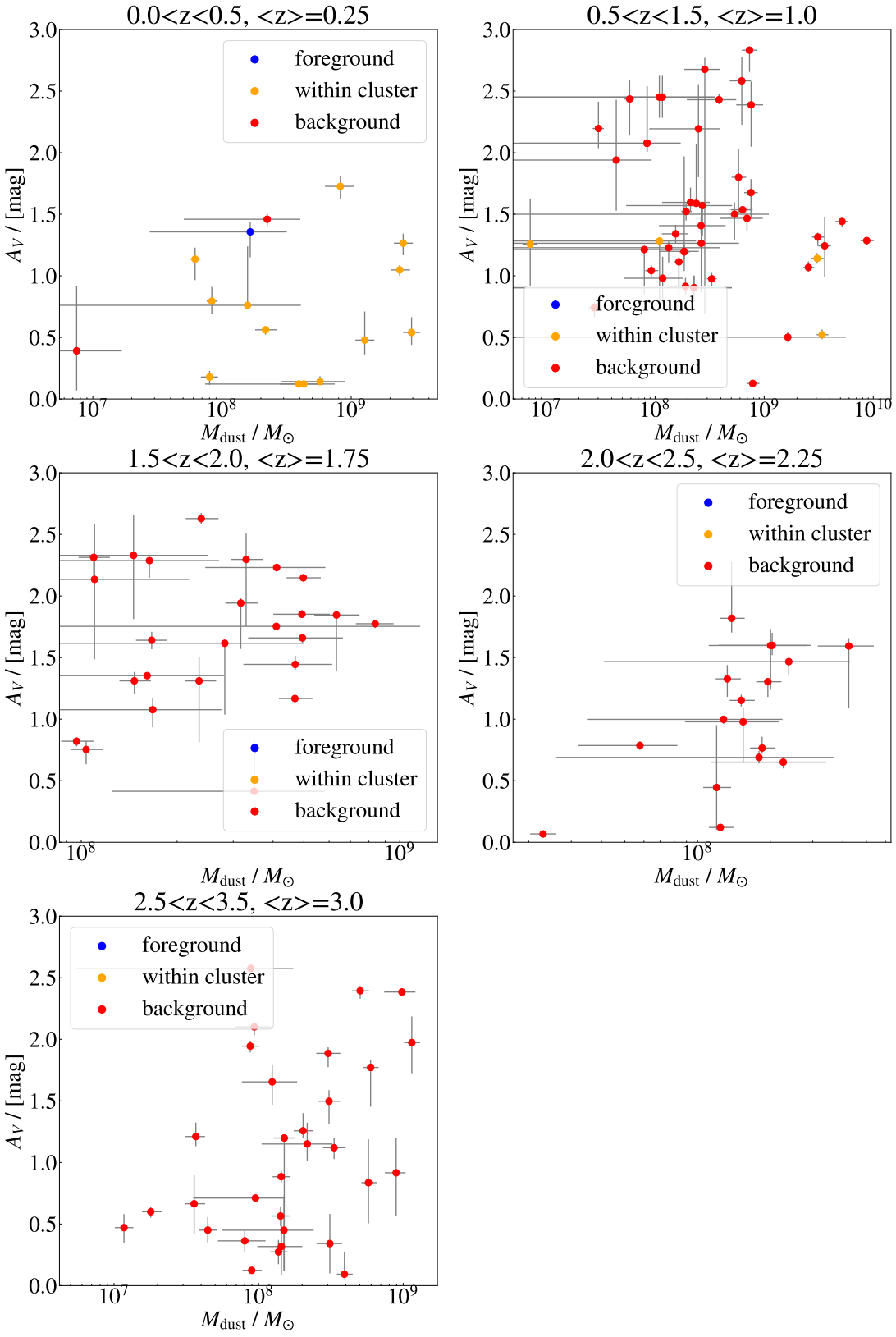

Figure 4.9: $A_V - M_{\rm dust}$ color-coded by position. Blue points are galaxies in the foreground, orange points are galaxies within clusters, and red points are galaxies behind the clusters.

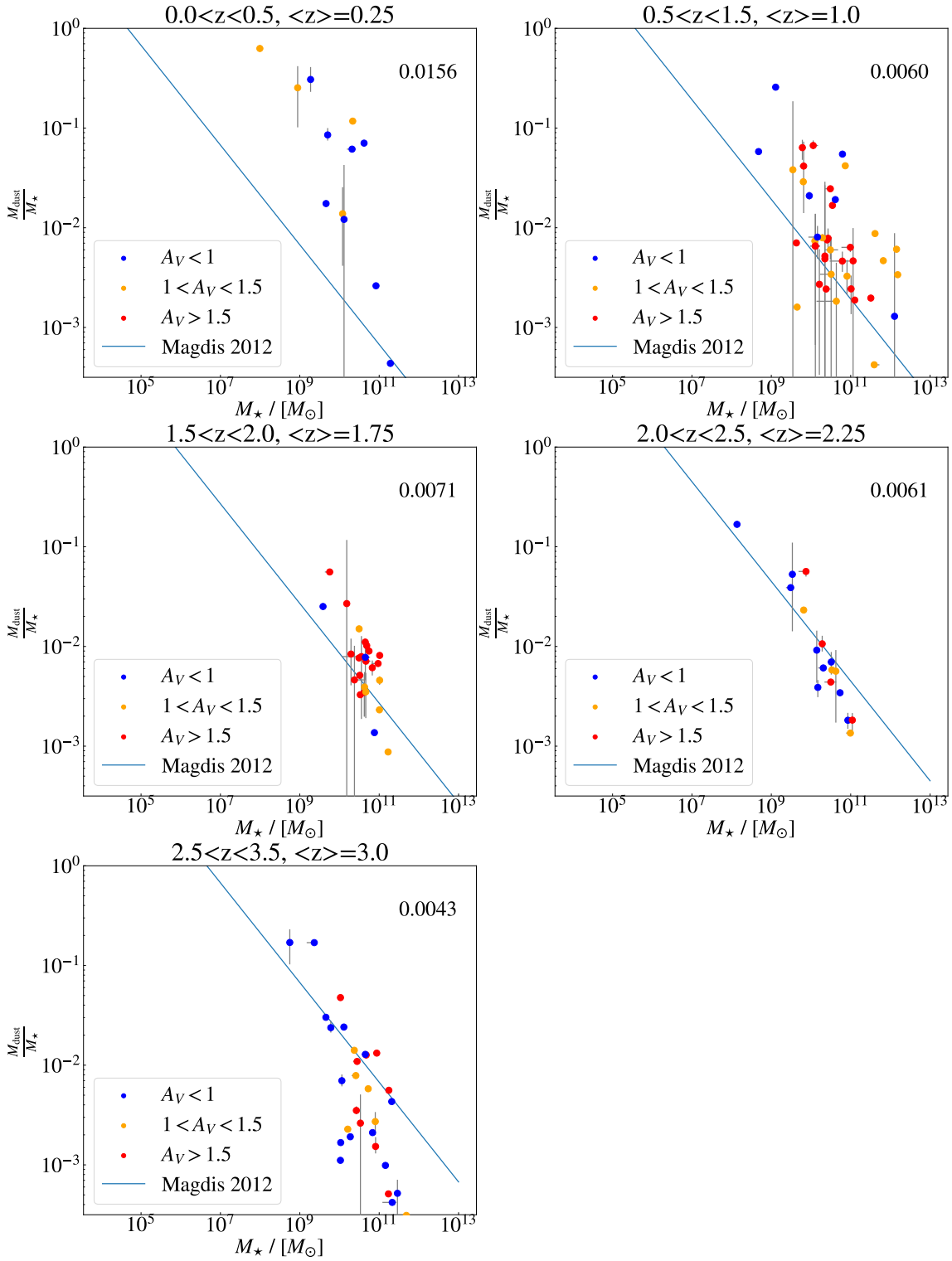

Figure 4.10: $M_{\rm dust}/M_\star - M_\star$ as function of z. The blue line indicate the $M_{\rm dust}/M_\star$ vs. $M_\star$ based on the result from Magdis *et al.*, 2012 by assuming $M_{\rm gas}/M_{\rm dust} \approx 100$. The median value of $M_{\rm dust}/M_\star$ in each bin is displayed at the upper-right corner.

4.5 Magnification and Depth

In this section we want to discuss how deep ALCS can go and how magnification helps us explore those faintest objects. We group $\mu(L_{\rm IR})$ into 5 redshift bins from $z = 0$ to $z = 5$ with an interval of 1. and we don't take galaxies at $z > 5$ int account, given the small number of samples at high redshift. We also indicate $\mu(L_{\rm IR})$ and $L_{\rm IR}$ of the faintest objects with arrows. It is worthy of note that at $0.5 < z < 1$ some galaxies residing in clusters have $\mu > 1$ (overlapping points in Fig. 4.11). This could be due to the difference in methods used to determine positions of galaxies, since V. Kokorev, G. Brammer *et al.* (in preparation) use $z_{\rm cl} - 0.1 < z_* < z_{\rm cl} + 0.1$ to make the judgment, while our assumption adds errors of $z_{\rm phot}$, which can be more inclusive. For galaxies with redshift close to the ones of clusters, i.e. they are likely within cluster, photometry can be a bit tricky because the high density of galaxies in the cluster makes it hard to accurately determine flux in apertures, which can introduce large error for SED fitting and deduction of $z_{\rm phot}$. Thus, using only $z_{\rm phot}$ may be more reliable for galaxies close to or within clusters.

By calculating the mean magnification factor $\langle\mu\rangle$ in each redshift bin, we know that the cluster lensing can roughly elevate observed flux by a factor of $\sim 3-5$. To obtain images with this enhanced quality, the observation of time should increase from t to $\mu^2 \cdot t$, which is a huge cost of exposure time. From the depth of the 90% completeness (black points) of $\mu(L_{\rm IR})$ we can see that it generally climb up with z, proving the effect of cosmological dimming. But there is still a discrepancy between our detection limits of $L_{\rm IR}$ and results from Wang *et al.*, 2021, since the μ might alter the trend as well and the number of samples is not large enough.

4.6 Comments on Measurements of Dust Mass and Infrared Luminosity

In this work we use flux at Rayleigh-Jeans tail of SED to calculate $M_{\rm dust}$, while using the integration of the whole SED to determine $L_{\rm IR}$. Thus, the 1.2 mm data we use should be able to constraint $M_{\rm dust}$ better than $L_{\rm IR}$. Schreiber *et al.*, 2018 explore the accuracy of monochromatic measurements (i,e, having only one far-infrared data point) of $L_{\rm IR}$. They found that $L_{\rm IR}$ is better determined when

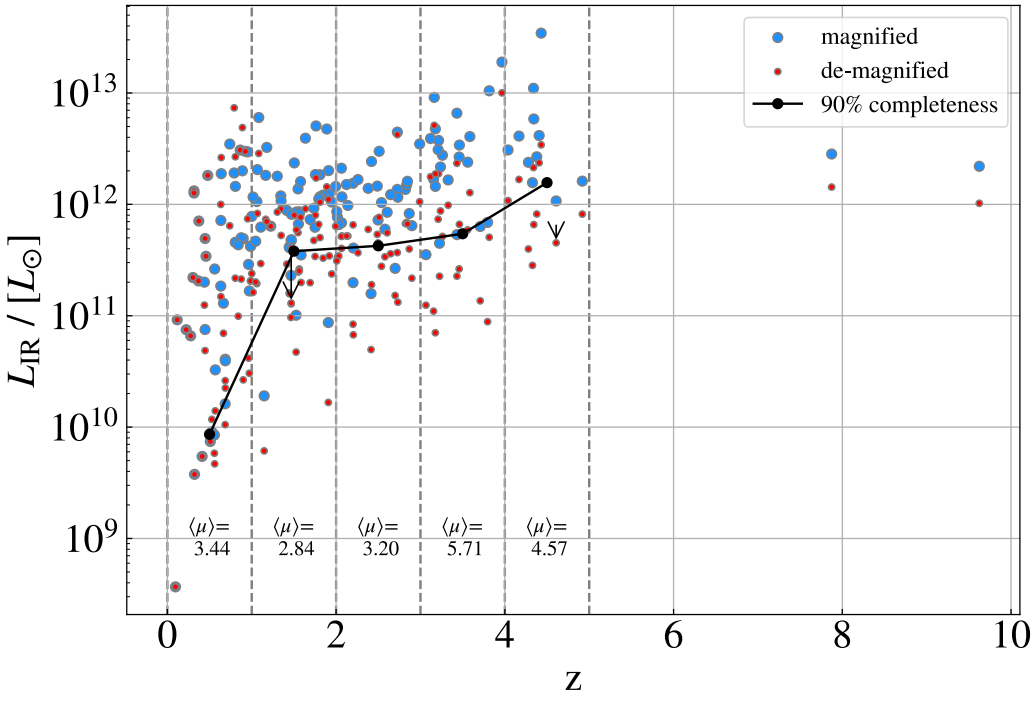

Figure 4.11: $\mu(L_{\rm IR})$ and $L_{\rm IR}$ vs. z. Galaxies with $L_{\rm IR} > 10^7 L_\odot$ are included. Blue points represent magnified luminosities while red points represent intrinsic luminosities. Dash grey lines are drawn to separate every bin and mean magnification factors $\langle\mu\rangle$ are displayed at the bottom of each bin. The black points are selected so that above these luminosities 90% of objects are included.

the data point probes rest-frame wavelength near the peak of SED. For objects at $z \sim 0$ and $z \sim 5$ in Schreiber *et al.*, 2018, deducing $L_{\rm IR}$ from single 1.1 mm flux introduces error of $L_{\rm IR}$ 0.3 dex and 0.2 dex respectively, while for $M_{\rm dust}$ the error is ~ 0.1 dex for all redshift. Thus they conclude that for a single ALMA data point, the calculated $L_{\rm IR}$ is very likely underestimated. In fact, according to their result based on mock data, for the band 6 (1.2 mm) of ALMA, $L_{\rm IR}$ can be measured with an error better than 0.2 dex only when $z > 5.7$, which is a blank in our samples. These results can partly account for our result in Section 4.2.3 that Some dusty galaxies with $A_V > 1.5$ merely reside in the main sequence, after including infrared luminosity.

4.7 Matched Counterparts Catalogue

The final catalogue (Table 4.1) contains photometric redshift, S/N of H band, and the other stellar properties deduced from UV/optical SED fitting from V. Kokorev, G. Brammer *et al.* (in preparation), plus $M_{\rm dust}$ and L from the infrared rescaled SED. Missing $M_{\rm dust}$ and $L_{\rm IR}$ due to negative 1.2 mm flux or $z_{\rm phot}$, and missing $\rm SNR_{F160W}$ due to missing flux and error of H band are set as blankness.

Table 4.1: Properties of ALMA sources and corresponding optical counterparts.

cluster	ID	RA	DEC	SNR_{F160W}	sep [arcsecond]	z_{phot}	SFR_{EAZY} $[\log(M_\odot/yr^{-1})]$	$M_\star$ $[\log(M_\odot)]$	A_V [mag]	$S_{1.2mm}$ [mJy]	M_{dust} $[\log(M_\odot)]$	L_{IR} $[\log(L_\odot)]$
ACTCLJ0102-49151	11	15.7477863	-49.2904001	26.63	2.75	2.61	$5.86^{+0.40}_{-0.34}$	$9.66^{+8.39}_{-8.47}$	$0.27^{+0.10}_{-0.10}$	0.35	$8.14^{+7.33}_{-7.23}$	$11.74^{+11.41}_{-11.27}$
ACTCLJ0102-49151	22	15.7626821	-49.2864566	4.77	1.85	1.34	$0.20^{+0.00}_{-0.00}$	$8.43^{+7.57}_{-7.51}$	$1.47^{+0.10}_{-0.10}$	0.96 ± 0.38	$8.84^{+8.44}_{-8.48}$	$11.96^{+11.86}_{-11.66}$
ACTCLJ0102-49151	50	15.7475095	-49.2821233	29.90	0.44	2.38	$0.22^{+0.12}_{-0.11}$	$9.53^{+8.12}_{-7.94}$	$0.69^{+0.05}_{-0.05}$	0.67 ± 0.61	$8.25^{+8.27}_{-8.19}$	$11.78^{+11.84}_{-11.72}$
ACTCLJ0102-49151	52	15.7561196	-49.2823856	47.54	0.15	2.02	$0.48^{+0.99}_{-0.41}$	$10.99^{+10.03}_{-10.33}$	$1.33^{+0.11}_{-0.15}$	0.40	$8.12^{+7.26}_{-7.14}$	$11.53^{+11.24}_{-11.04}$
ACTCLJ0102-49151	118	15.7128798	-49.2607919	15.35	0.41	4.34	$24.83^{+2.71}_{-1.90}$	$10.28^{+9.15}_{-8.97}$	$2.12^{+0.27}_{-0.31}$	2.93 ± 0.13	$8.23^{+7.61}_{-7.50}$	$12.33^{+12.02}_{-11.84}$
ACTCLJ0102-49151	160	15.7508527	-49.2677044	54.76	0.39	1.99	$11.86^{+-0.58}_{-4.94}$	$10.55_{-10.38}$	$1.62^{+-0.15}_{-0.58}$	0.87 ± 0.63	$8.45^{+8.34}_{-8.33}$	$11.80^{+11.85}_{-11.68}$
ACTCLJ0102-49151	215	15.7288441	-49.2540865	268.50	1.61	0.86	$0.05^{+0.00}_{-0.00}$	$10.79^{+8.96}_{-8.87}$	$0.52^{+0.04}_{-0.04}$	3.60 ± 0.12	$9.53^{+8.68}_{-8.58}$	$12.49^{+12.34}_{-12.06}$
ACTCLJ0102-49151	223	15.7051647	-49.2524655	48.09	0.66	2.20	$38.27^{+2.95}_{-16.14}$	$10.63^{+8.73}_{-9.74}$	$1.47^{+0.00}_{-0.11}$	0.78 ± 0.63	$8.38^{+8.28}_{-8.30}$	$11.82^{+11.90}_{-11.73}$
ACTCLJ0102-49151	224	15.7320137	-49.2525191	4.46	1.28	4.43	$0.49^{+0.35}_{-0.49}$	$10.09^{+9.29}_{-9.72}$	$2.56^{+0.04}_{-0.23}$	8.99 ± 0.10	$8.41^{+7.76}_{-7.65}$	$12.53^{+12.19}_{-12.03}$
ACTCLJ0102-49151	241	15.7422060	-49.2489458	47.94	0.06	2.82	$0.78^{+0.42}_{-0.29}$	$11.16^{+9.59}_{-9.66}$	$0.57^{+0.08}_{-0.09}$	0.53	$8.15^{+7.37}_{-7.25}$	$11.83^{+11.52}_{-11.35}$
ACTCLJ0102-49151	251	15.7294397	-49.2386615	6.93	2.00	0.37	$0.00^{+0.00}_{-0.00}$	$7.95^{+-7.83}$	$0.12^{+0.00}_{-0.00}$	0.74 ± 0.64	$8.60^{+8.55}_{-8.51}$	$11.31^{+11.42}_{-11.24}$
ACTCLJ0102-49151	276	15.7053793	-49.2439317	11.62	0.24	3.46	$12.69^{+0.15}_{-0.11}$	$10.42^{+9.43}_{-9.54}$	$2.10^{+0.05}_{-0.07}$	1.16 ± 0.28	$7.97^{+7.46}_{-7.40}$	$11.82^{+11.58}_{-11.36}$
ACTCLJ0102-49151	294	15.7056994	-49.2514717	293.83	0.73	0.93	$0.05^{+0.00}_{-0.00}$	$10.86^{+9.25}_{-9.22}$	$1.14^{+0.04}_{-0.04}$	3.16 ± 0.15	$9.49^{+8.66}_{-8.59}$	$12.48^{+12.23}_{-12.05}$
ACTCLJ0102-49151	128	15.7103067	-49.2615949	127.31	0.08	2.90	$0.20^{+0.01}_{-0.01}$	$11.25^{+9.70}_{-9.65}$	$0.45^{+0.11}_{-0.10}$	0.25	$7.65^{+6.86}_{-6.77}$	$11.34^{+11.01}_{-10.86}$
AbellS1063	15	342.1940949	-44.5130180	71.68	0.41	1.35	$0.66^{+0.25}_{-0.19}$	$9.78^{+8.79}_{-8.65}$	$2.43^{+0.04}_{-0.04}$	0.84 ± 0.40	$8.59^{+8.23}_{-8.28}$	$11.72^{+11.65}_{-11.45}$
AbellS1063	17	342.1970228	-44.5133754	152.71	0.13	1.55	$13.71^{+8.40}_{-10.48}$	$10.67^{+10.14}_{-10.00}$	$2.30^{+0.21}_{-0.55}$	0.91	$8.52^{+7.62}_{-7.54}$	$11.75^{+11.50}_{-11.31}$
AbellS1063	147	342.1742360	-44.5326395	592.02	1.13	0.63	$15.99^{+4.96}_{-2.88}$	$10.43^{+9.11}_{-9.31}$	$1.60^{+0.12}_{-0.08}$	1.23 ± 0.56	$8.32^{+8.02}_{-7.98}$	$11.17^{+11.14}_{-10.92}$
AbellS1063	222	342.2044085	-44.5403889	31.95	0.08	3.97	$0.96^{+3.32}_{-0.84}$	$11.08^{+10.07}_{-10.07}$	$1.79^{+0.09}_{-0.10}$	5.42 ± 0.08	$8.99^{+8.32}_{-8.18}$	$13.00^{+12.63}_{-12.51}$
Abell209	38	22.9724037	-13.6214995	35.38	0.29	2.06	$3.67^{+0.93}_{-0.73}$	$9.82^{+8.48}_{-8.55}$	$1.15^{+0.05}_{-0.05}$	0.35	$8.18^{+7.32}_{-7.20}$	$11.60^{+11.29}_{-11.14}$
Abell2163	11	243.9543963	-6.1372017	59.83	0.23	1.92	$36.47^{+1.40}_{-1.84}$	$10.29^{+8.80}_{-9.35}$	$2.29^{+0.02}_{-0.14}$	0.75 ± 0.53	$8.21^{+8.03}_{-8.07}$	$11.54^{+11.56}_{-11.39}$

Table 4.1: Properties of ALMA sources and corresponding optical counterparts.

cluster	ID	RA	DEC	SNR_{F160W}	sep [arcsecond]	z_{phot}	SFR_{EAZY} $[\log(M_\odot/yr^{-1})]$	$M_\star$ $[\log(M_\odot)]$	A_V [mag]	$S_{1.2mm}$ [mJy]	M_{dust} $[\log(M_\odot)]$	L_{IR} $[\log(L_\odot)]$
Abell2537	42	347.1017953	-2.1848524	326.64	0.25	1.00	$12.42^{+18.13}_{-12.38}$	$11.01^{+10.19}_{-10.36}$	$2.19^{+0.36}_{-0.39}$	0.84 ± 0.54	$8.40^{+8.17}_{-8.21}$	$11.38^{+11.39}_{-11.21}$
Abell2537	49	347.0746776	-2.1868689	...	0.13	1.69	$0.14^{+0.00}_{-0.01}$	$10.88^{+9.73}_{-9.14}$	$0.75^{+0.07}_{-0.12}$	0.45	$8.02^{+7.14}_{-7.04}$	$11.30^{+11.06}_{-10.83}$
Abell2537	66	347.0820153	-2.1903513	151.55	0.17	3.16	$32.35^{+2.47}_{-2.56}$	$10.03^{+8.27}_{-8.56}$	$0.60^{+0.04}_{-0.05}$	0.58	$7.25^{+6.53}_{-6.37}$	$11.04^{+10.71}_{-10.59}$
Abell2537	6	347.0866914	-2.1762725	261.34	0.75	0.45	$0.16^{+0.11}_{-0.15}$	$9.66^{+8.32}_{-8.46}$	$0.18^{+0.05}_{-0.07}$	0.19	$7.90^{+7.11}_{-7.06}$	$10.69^{+10.48}_{-10.27}$
Abell2537	24	347.0881901	-2.1817937	148.38	0.51	3.18	$18.67^{+8.13}_{-6.91}$	$10.02^{+9.02}_{-9.03}$	$0.47^{+0.11}_{-0.12}$	0.51	$7.07^{+6.28}_{-6.20}$	$10.85^{+10.52}_{-10.34}$
Abell2744	7	3.5796823	-30.3783961	65.89	0.07	2.14	$0.03^{+0.00}_{-0.00}$	$10.73^{+9.09}_{-8.77}$	$0.77^{+0.09}_{-0.05}$	0.48	$8.27^{+7.40}_{-7.30}$	$11.72^{+11.40}_{-11.25}$
Abell2744	21	3.5920469	-30.3804818	38.80	0.26	7.87	$391.12^{+75.66}_{-73.64}$	$12.99^{+12.33}_{-12.32}$	$2.65^{+0.05}_{-0.08}$	0.42 ± 0.27	$7.28^{+7.18}_{-7.12}$	$12.16^{+12.13}_{-11.99}$
Abell2744	33	3.5850158	-30.3818137	74.17	0.05	3.12	$41.81^{+17.70}_{-15.14}$	$10.72^{+9.24}_{-9.68}$	$1.50^{+0.09}_{-0.18}$	1.41 ± 0.11	$8.49^{+7.77}_{-7.69}$	$12.25^{+11.99}_{-11.74}$
Abell2744	56	3.5732619	-30.3835090	163.44	0.14	1.42	$18.94^{+3.19}_{-2.69}$	$10.41^{+8.94}_{-9.09}$	$1.52^{+0.07}_{-0.07}$	0.63	$8.28^{+7.39}_{-7.27}$	$11.46^{+11.22}_{-11.01}$
Abell2744	81	3.5825059	-30.3854775	68.60	0.15	2.99	$0.91^{+7.02}_{--0.28}$	$10.41^{+9.68}_{-9.75}$	$1.26^{+0.14}_{-0.06}$	1.31	$8.31^{+7.56}_{-7.45}$	$12.02^{+11.74}_{-11.55}$
Abell2744	319	3.5760949	-30.4131819	45.08	0.86	3.21	$19.84^{+1.01}_{-1.59}$	$10.44^{+9.43}_{-9.76}$	$1.89^{+0.05}_{-0.11}$	1.31 ± 0.12	$8.48^{+7.81}_{-7.72}$	$12.28^{+12.02}_{-11.79}$
Abell2744	17	3.5813087	-30.3801650	19.16	0.50	2.87	$4.08^{+0.29}_{-0.26}$	$10.53^{+9.37}_{-9.35}$	$2.58^{+0.03}_{-0.03}$	0.34 ± 0.33	$7.95^{+7.93}_{-7.92}$	$11.60^{+11.70}_{-11.58}$
Abell2744	47	3.5720304	-30.3829544	109.34	0.15	1.55	$9.59^{+11.13}_{-8.55}$	$10.62^{+9.90}_{-9.95}$	$2.33^{+0.33}_{-0.52}$	0.43 ± 0.32	$8.16^{+8.02}_{-7.97}$	$11.39^{+11.40}_{-11.24}$
Abell2744	176	3.5723343	-30.3959509	143.51	0.87	0.44	$0.21^{+0.01}_{-0.02}$	$8.95^{+6.99}_{-7.03}$	$1.46^{+0.05}_{-0.05}$	0.58 ± 0.46	$8.35^{+8.26}_{-8.24}$	$11.10^{+11.16}_{-11.00}$
Abell2744	178	3.6005008	-30.3961199	153.08	0.45	1.11	$4.24^{+0.70}_{-1.60}$	$9.82^{+8.38}_{-9.14}$	$1.57^{+-0.04}_{-0.24}$	0.58 ± 0.49	$8.43^{+8.37}_{-8.34}$	$11.47^{+11.53}_{-11.38}$
Abell2744	227	3.5690078	-30.4027867	125.98	0.26	2.58	$28.60^{+9.11}_{-7.62}$	$11.23^{+9.97}_{-9.93}$	$1.94^{+0.04}_{-0.05}$	0.26	$7.94^{+7.11}_{-7.03}$	$11.53^{+11.26}_{-11.01}$
AbellS295	9	41.4026213	-53.0576036	...	2.98	4.28	$0.81^{+0.00}_{-0.00}$	$8.74^{+8.30}_{-8.19}$	$0.93^{+0.25}_{-0.27}$	0.63	$7.50^{+6.84}_{-6.70}$	$11.60^{+11.23}_{-11.10}$
Abell3192	31	59.7084164	-29.9418886	223.13	0.09	1.76	$60.34^{+2.01}_{-1.54}$	$11.01^{+9.67}_{-9.67}$	$1.77^{+0.03}_{-0.04}$	2.94 ± 0.23	$8.92^{+8.08}_{-8.04}$	$12.24^{+11.95}_{-11.79}$
Abell3192	40	59.7130272	-29.9196827	40.63	0.10	3.43	$5.12^{+5.29}_{-4.03}$	$10.37^{+9.09}_{-9.23}$	$1.12^{+0.08}_{-0.09}$	2.20 ± 0.14	$8.52^{+7.83}_{-7.73}$	$12.37^{+12.07}_{-11.89}$
Abell3192	131	59.6984479	-29.9426520	...	2.12	2.26	$0.76^{+2.72}_{-0.75}$	$9.49^{+8.07}_{-8.87}$	$0.45^{+0.51}_{-0.34}$	0.79	$8.08^{+7.25}_{-7.16}$	$11.57^{+11.31}_{-11.11}$

Table 4.1: Properties of ALMA sources and corresponding optical counterparts.

cluster	ID	RA	DEC	SNR_{F160W}	sep [arcsecond]	z_{phot}	SFR_{EAZY} $[\log(M_\odot/yr^{-1})]$	$M_\star$ $[\log(M_\odot)]$	A_V [mag]	$S_{1.2mm}$ [mJy]	M_{dust} $[\log(M_\odot)]$	L_{IR} $[\log(L_\odot)]$
Abell3192	138	59.7380434	-29.9148732	...	0.36	3.46	$8.10^{+4.71}_{-3.17}$	$10.27^{+9.17}_{-9.11}$	$0.66^{+0.23}_{-0.24}$	0.87	$7.55^{+6.84}_{-6.70}$	$11.42^{+11.08}_{-10.93}$
Abell3192	83	59.7246463	-29.9320537	697.56	0.07	0.63	$1.02^{+0.00}_{-0.00}$	$12.10^{+10.29}_{-10.20}$	$0.50^{+0.05}_{-0.04}$	0.33 ± 0.88	$9.22^{+9.60}_{-9.61}$	$12.00^{+12.50}_{-12.41}$
Abell3192	154	59.7362229	-29.9055828	...	1.07	3.33	$11.60^{+-6.29}_{-10.48}$	$11.68_{-11.37}$	$1.20^{+-0.34}_{-1.08}$	0.57	$8.18^{+7.46}_{-7.37}$	$11.99^{+11.71}_{-11.52}$
Abell370	18	39.9591641	-1.5950176	84.13	0.15	2.49	$0.04^{+0.03}_{-0.01}$	$10.93^{+10.18}$	$0.98^{+0.11}_{-0.33}$	0.67 ± 0.27	$8.19^{+7.80}_{-7.82}$	$11.73^{+11.60}_{-11.39}$
Abell370	31	39.9767810	-1.5601292	615.23	0.41	0.22	$2.26^{+0.27}_{-0.62}$	$10.08^{+8.35}_{-9.09}$	$1.36^{+0.08}_{-0.21}$	0.58 ± 0.48	$8.22^{+8.18}_{-8.14}$	$10.87^{+11.00}_{-10.80}$
Abell370	103	39.9923102	-1.5734715	288.19	0.10	1.23	$99.12^{+13.18}_{-35.23}$	$11.06^{+9.82}_{-10.28}$	$1.50^{+0.10}_{-0.21}$	0.57 ± 0.61	$8.73^{+8.76}_{-8.77}$	$11.80^{+11.98}_{-11.85}$
Abell370	110	39.9856890	-1.5739784	632.80	0.07	1.17	$26.09^{+4.11}_{-2.95}$	$11.51^{+9.94}_{-9.95}$	$1.54^{+0.03}_{-0.03}$	1.59 ± 0.33	$8.80^{+8.18}_{-8.15}$	$11.87^{+11.66}_{-11.45}$
Abell370	146	39.9643502	-1.5782083	220.40	0.23	0.96	$1.74^{+3.07}_{-1.63}$	$10.21^{+9.49}_{-9.54}$	$1.94^{+0.49}_{-0.41}$	0.35 ± 0.32	$7.64^{+7.69}_{-7.61}$	$10.62^{+10.78}_{-10.58}$
Abell370	27	39.9730709	-1.5597934	110.24	0.61	3.26	$13.86^{+3.99}_{-4.14}$	$10.06^{+8.78}_{-8.75}$	$0.36^{+0.08}_{-0.09}$	0.94 ± 0.34	$7.90^{+7.50}_{-7.45}$	$11.71^{+11.54}_{-11.38}$
Abell370	172	39.9473985	-1.5814055	44.43	1.09	0.24	$0.13^{+0.02}_{-0.01}$	$8.59^{+7.22}_{-7.37}$	$0.12^{+0.03}_{-0.02}$	-0.17	...	...
Abell383	40	42.0141300	-3.5291164	1448.29	0.79	0.12	$0.04^{+0.00}_{-0.00}$	$10.92^{+9.36}_{-9.47}$	$0.56^{+0.03}_{-0.04}$	2.07	$8.34^{+7.69}_{-7.57}$	$10.96^{+10.80}_{-10.58}$
Abell383	24	42.0117763	-3.5240168	13.58	1.12	2.73	$1.99^{+0.08}_{-0.08}$	$8.75^{+7.41}_{-7.41}$	$0.71^{+0.02}_{-0.02}$	0.60 ± 0.35	$7.98^{+7.75}_{-7.78}$	$11.57^{+11.57}_{-11.37}$
Abell383	50	42.0117548	-3.5326342	90.91	0.56	0.90	$0.64^{+0.18}_{-0.20}$	$8.68^{+7.83}_{-7.71}$	$0.74^{+0.04}_{-0.08}$	0.54	$7.44^{+6.57}_{-6.49}$	$10.42^{+10.23}_{-10.01}$
MACSJ0035.4-2015	68	8.8781846	-20.2652598	4.99	0.41	4.04	$2.89^{+0.23}_{-0.48}$	$9.76^{+9.81}_{-8.19}$	$1.01^{+0.96}_{-0.52}$	0.86	$8.00^{+7.32}_{-7.18}$	$12.03^{+11.66}_{-11.53}$
MACSJ0035.4-2015	94	8.8635169	-20.2715042	603.97	0.33	0.28	$7.67^{+10.61}_{--0.08}$	$10.11^{+9.02}_{-9.17}$	$0.76^{+0.48}_{--0.07}$	0.42 ± 0.65	$8.20^{+8.40}_{-8.39}$	$10.82^{+11.19}_{-11.06}$
MACSJ0035.4-2015	33	8.8562578	-20.2581929	195.24	0.31	1.06	$1.85^{+0.03}_{-0.03}$	$9.51^{+8.38}_{-8.22}$	$1.44^{+0.06}_{-0.05}$	-0.09	...	...
MACSJ0159.8-0849	5	29.9653751	-8.8194848	109.11	0.26	1.30	$9.50^{+10.37}_{-6.62}$	$10.99_{-10.60}$	$2.58^{+0.20}_{-0.36}$	1.38 ± 0.28	$8.79^{+8.13}_{-8.15}$	$11.93^{+11.71}_{-11.52}$
MACSJ0159.8-0849	24	29.9472208	-8.8258977	266.28	0.51	0.66	$0.03^{+0.00}_{-0.00}$	$10.10^{+8.63}_{-8.60}$	$1.04^{+0.04}_{-0.05}$	0.20	$7.97^{+7.16}_{-7.04}$	$10.84^{+10.67}_{-10.44}$
MACSJ0159.8-0849	46	29.9556285	-8.8330682	686.55	0.25	0.89	$1391.59^{+286.77}_{-293.03}$	$12.18^{+10.69}_{-10.94}$	$1.44^{+0.02}_{-0.05}$	2.22 ± 0.12	$9.71^{+8.87}_{-8.83}$	$12.69^{+12.51}_{-12.28}$
MACSJ0159.8-0849	61	29.9648314	-8.8370309	415.87	0.14	0.88	$0.99^{+14.63}_{-0.95}$	$11.10^{+10.10}_{-10.22}$	$1.59^{+0.48}_{-0.01}$	0.58	$8.38^{+7.51}_{-7.42}$	$11.33^{+11.15}_{-10.87}$

Table 4.1: Properties of ALMA sources and corresponding optical counterparts.

cluster	ID	RA	DEC	SNR_{F160W}	sep [arcsecond]	z_{phot}	SFR_{EAZY} $[\log(M_\odot/yr^{-1})]$	$M_\star$ $[\log(M_\odot)]$	A_V [mag]	$S_{1.2mm}$ [mJy]	M_{dust} $[\log(M_\odot)]$	L_{IR} $[\log(L_\odot)]$
MACSJ0257.1-2325	13	44.2968806	-23.4287678	20.88	0.33	2.73	$33.36^{+0.27}_{-0.34}$	$11.24^{+10.10}_{-9.99}$	$2.38^{+0.03}_{-0.03}$	1.83 ± 0.36	$8.99^{+8.37}_{-8.38}$	$12.63^{+12.36}_{-12.18}$
MACS0329.7-0211	11	52.4239873	-2.1824407	336.01	0.09	2.84	$103.10^{+0.48}_{-0.61}$	$10.83^{+9.50}_{-9.55}$	$0.88^{+0.05}_{-0.05}$	0.58	$8.16^{+7.36}_{-7.27}$	$11.84^{+11.49}_{-11.36}$
MACSJ0416.1-2403	51	64.0290222	-24.0666569	159.87	0.04	2.07	$65.67^{+5.87}_{-22.25}$	$10.53^{+9.66}_{-9.68}$	$1.30^{+0.01}_{-0.12}$	0.59	$8.29^{+7.43}_{-7.31}$	$11.72^{+11.41}_{-11.25}$
MACSJ0416.1-2403	79	64.0486442	-24.0720833	109.30	0.21	2.03	$34.32^{+7.50}_{-4.65}$	$10.50^{+10.07}_{-9.98}$	$1.82^{+0.46}_{-0.12}$	0.35	$8.14^{+7.26}_{-7.16}$	$11.54^{+11.27}_{-11.06}$
MACSJ0416.1-2403	117	64.0449843	-24.0798771	271.18	0.05	1.91	$34.16^{+0.01}_{-0.01}$	$10.49^{+9.03}_{-8.96}$	$1.17^{+0.03}_{-0.02}$	1.08	$8.67^{+7.80}_{-7.71}$	$12.04^{+11.80}_{-11.59}$
MACSJ0416.1-2403	160	64.0367835	-24.0895812	85.55	0.10	1.75	$0.05^{+0.14}_{-0.03}$	$10.51^{+9.30}_{-9.56}$	$1.64^{+0.07}_{-0.07}$	0.36	$8.22^{+7.30}_{-7.25}$	$11.53^{+11.26}_{-11.08}$
MACSJ0416.1-2403	120	64.0437953	-24.0802677	23.85	0.44	9.62	$214.17^{+18.19}_{-19.23}$	$13.43^{+12.18}_{-12.15}$	$2.85^{+0.00}_{-0.00}$	0.23	$6.80^{+6.36}_{-6.26}$	$12.01^{+11.65}_{-11.44}$
MACSJ0416.1-2403	138	64.0438489	-24.0846586	97.50	0.53	2.50	$30.64^{+0.72}_{-0.62}$	$10.14^{+8.85}_{-8.96}$	$1.00^{+0.03}_{-0.04}$	0.34 ± 0.24	$8.11^{+7.99}_{-7.97}$	$11.65^{+11.65}_{-11.53}$
MACSJ0416.1-2403	156	64.0366134	-24.0882085	109.50	0.15	1.58	$17.28^{+0.63}_{-3.88}$	$10.52^{+9.78}_{-8.36}$	$2.31^{+0.02}_{-0.20}$	0.22	$8.04^{+7.14}_{-7.06}$	$11.30^{+11.05}_{-10.87}$
MACSJ0417.5-1154	46	64.3888354	-11.9175841	529.72	1.52	0.48	$0.97^{+0.35}_{-0.27}$	$10.62^{+9.31}_{-9.34}$	$0.54^{+0.12}_{-0.10}$	4.30	$9.47^{+8.69}_{-8.61}$	$12.26^{+12.06}_{-11.85}$
MACSJ0417.5-1154	49	64.4172807	-11.9168995	...	1.65	3.16	$2.11^{+1.02}_{-1.41}$	$11.32^{+10.15}_{-10.56}$	$0.92^{+0.29}_{-0.35}$	3.32 ± 0.16	$8.95^{+8.16}_{-8.17}$	$12.71^{+12.44}_{-12.21}$
MACSJ0417.5-1154	218	64.3833817	-11.8826035	17.85	1.84	0.45	$0.43^{+0.04}_{-0.05}$	$8.23^{+7.09}_{-7.34}$	$1.73^{+0.09}_{-0.10}$	1.29 ± 0.25	$8.92^{+8.36}_{-8.29}$	$11.69^{+11.57}_{-11.33}$
MACSJ0417.5-1154	221	64.3853268	-11.8841190	201.90	0.39	1.85	$80.35^{+1.96}_{-2.26}$	$10.66^{+9.28}_{-9.38}$	$1.35^{+0.02}_{-0.03}$	0.75 ± 0.52	$8.21^{+8.08}_{-8.03}$	$11.52^{+11.53}_{-11.34}$
MACSJ0417.5-1154	223	64.3856046	-11.8847084	128.30	0.17	1.07	$6.89^{+2.19}_{-3.60}$	$10.06^{+9.56}_{-9.10}$	$2.39^{+0.19}_{-0.34}$	1.93 ± 0.49	$8.88^{+8.34}_{-8.31}$	$11.92^{+11.76}_{-11.53}$
MACS0429.6-0253	4	67.3958701	-2.8775789	17.68	0.33	2.51	$1.82^{+0.55}_{-0.43}$	$10.90^{+9.65}_{-9.50}$	$1.15^{+0.17}_{-0.14}$	1.37 ± 0.68	$8.34^{+8.03}_{-8.05}$	$11.88^{+11.78}_{-11.62}$
MACS0429.6-0253	19	67.4001178	-2.8852218	696.83	0.13	0.79	$2000.18^{+27.66}_{-19.00}$	$12.16^{+10.75}_{-10.84}$	$1.29^{+0.02}_{-0.03}$	2.45	$9.94^{+9.15}_{-9.03}$	$12.87^{+12.66}_{-12.46}$
MACS0429.6-0253	27	67.4046007	-2.8931148	35.13	0.77	3.21	$47.35^{+17.74}_{-14.28}$	$10.91^{+9.66}_{-9.70}$	$1.65^{+0.14}_{-0.19}$	1.14 ± 0.45	$8.09^{+7.78}_{-7.68}$	$11.87^{+11.73}_{-11.52}$
MACSJ0553.4-3342	58	88.3757309	-33.6978091	...	0.15	1.74	$0.04^{+0.01}_{-0.01}$	$11.01^{+10.19}_{-10.25}$	$1.31^{+0.20}_{-0.50}$	0.54	$8.37^{+7.49}_{-7.36}$	$11.68^{+11.38}_{-11.22}$
MACSJ0553.4-3342	61	88.3395244	-33.6985393	236.37	0.17	1.58	$40.26^{+6.43}_{-4.81}$	$11.01^{+9.61}_{-9.52}$	$1.44^{+0.07}_{-0.04}$	1.10 ± 0.31	$8.67^{+8.16}_{-8.17}$	$11.88^{+11.72}_{-11.49}$
MACSJ0553.4-3342	67	88.3720848	-33.6989820	2.56	0.76	3.24	$0.63^{+0.49}_{-0.44}$	$9.78^{+8.97}_{-8.83}$	$0.32^{+0.27}_{-0.23}$	0.79 ± 0.24	$8.16^{+7.76}_{-7.66}$	$11.94^{+11.75}_{-11.54}$

Table 4.1: Properties of ALMA sources and corresponding optical counterparts.

cluster	ID	RA	DEC	SNR_{F160W}	sep [arcsecond]	z_{phot}	SFR_{EAZY} $[\log(M_\odot/yr^{-1})]$	$M_\star$ $[\log(M_\odot)]$	A_V [mag]	$S_{1.2mm}$ [mJy]	M_{dust} $[\log(M_\odot)]$	L_{IR} $[\log(L_\odot)]$
MACSJ0553.4-3342	133	88.3657754	-33.7044538	198.61	0.05	1.18	$5.21^{+3.81}_{-3.42}$	$10.54^{+9.37}_{-9.60}$	$1.80^{+0.23}_{-0.29}$	2.80 ± 0.27	$8.77^{+8.01}_{-7.90}$	$11.85^{+11.66}_{-11.41}$
MACSJ0553.4-3342	190	88.3660559	-33.7084931	936.37	0.34	0.74	$0.04^{+0.00}_{-0.00}$	$10.61^{+8.98}_{-9.09}$	$0.13^{+0.00}_{-0.00}$	4.74	$8.89^{+8.08}_{-7.98}$	$11.81^{+11.61}_{-11.38}$
MACSJ0553.4-3342	249	88.3651136	-33.7121852	184.94	0.21	0.95	$2.22^{+3.73}_{-0.81}$	$10.49_{-9.92}$	$1.68^{+0.11}_{-0.21}$	3.11 ± 0.21	$8.88^{+8.07}_{-8.00}$	$11.87^{+11.67}_{-11.45}$
MACSJ0553.4-3342	275	88.3585617	-33.7143380	401.73	0.19	0.80	$2.60^{+3.02}_{-2.21}$	$10.91^{+9.31}_{-9.39}$	$1.41^{+0.07}_{-0.07}$	0.60 ± 0.37	$8.42^{+8.25}_{-8.19}$	$11.34^{+11.39}_{-11.13}$
MACSJ0553.4-3342	355	88.3469942	-33.7210992	100.47	0.18	1.81	$35.27^{+1.23}_{-1.09}$	$10.69^{+9.28}_{-9.47}$	$1.66^{+0.03}_{-0.04}$	1.07 ± 0.33	$8.69^{+8.23}_{-8.21}$	$12.02^{+11.86}_{-11.64}$
MACSJ0553.4-3342	398	88.3744572	-33.7238804	...	1.03	4.41	$21.14^{+4.32}_{-4.37}$	$11.70^{+10.89}_{-11.00}$	$2.26^{+0.18}_{-0.30}$	1.09	$8.25^{+7.60}_{-7.49}$	$12.37^{+12.02}_{-11.87}$
MACS1115.9+0129	2	168.9612161	1.5098552	85.27	0.29	3.17	$56.95^{+13.28}_{-12.19}$	$11.47^{+10.37}_{-10.31}$	$1.97^{+0.10}_{-0.09}$	-3.34	...	...
MACS1115.9+0129	4	168.9668036	1.5078324	205.52	0.54	2.41	$55.96^{+0.21}_{-0.19}$	$10.51^{+9.19}_{-9.25}$	$0.65^{+0.04}_{-0.05}$	0.73 ± 0.36	$8.35^{+8.06}_{-8.05}$	$10.70^{+10.46}_{-10.39}$
MACS1115.9+0129	34	168.9756027	1.4989589	125.66	2.39	0.69	$1.15^{+0.68}_{-0.54}$	$9.11^{+8.03}_{-8.00}$	$0.98^{+0.05}_{-0.06}$	1.34	$8.52^{+7.57}_{-7.50}$	$10.42^{+9.73}_{-9.66}$
MACS1115.9+0129	36	168.9662300	1.4985808	837.82	0.15	0.53	$44.10^{+9.95}_{-26.26}$	$11.59^{+11.14}$	$1.11^{+0.03}_{-0.43}$	0.47	$8.22^{+7.22}_{-7.18}$	$10.07^{+9.37}_{-9.28}$
MACS1115.9+0129	33	168.9764012	1.4992074	174.17	0.54	0.69	$2.31^{+1.53}_{-1.37}$	$9.54^{+8.40}_{-8.69}$	$1.23^{+0.05}_{-0.12}$	0.59 ± 1.10	$8.12^{+8.42}_{-8.40}$	$10.02^{+10.33}_{-10.30}$
MACSJ1149.5+2223	77	177.4004340	22.4067990	299.76	0.22	1.56	$27.50^{+11.01}_{-13.40}$	$10.63^{+9.41}_{-9.17}$	$1.08^{+0.09}_{-0.14}$	0.62 ± 0.43	$8.22^{+8.03}_{-8.07}$	$11.42^{+11.44}_{-11.28}$
MACSJ1149.5+2223	229	177.3918136	22.3879592	19.48	0.89	1.47	$0.05^{+0.04}_{-0.03}$	$8.01^{+7.05}_{-7.00}$	$1.26^{+0.32}_{-0.40}$	0.59 ± 0.66	$8.42^{+8.51}_{-8.48}$	$11.61^{+11.78}_{-11.66}$
MACSJ1149.5+2223	27	177.4166485	22.4158657	30.41	0.03	4.61	$0.12^{+0.20}_{-0.07}$	$9.84^{+8.84}_{-8.47}$	$0.06^{+0.01}_{-0.00}$	0.27	$7.47^{+6.85}_{-6.75}$	$11.65^{+11.32}_{-11.16}$
MACSJ1149.5+2223	95	177.4210623	22.4046942	86.88	0.63	1.53	$9.82^{+0.26}_{-0.33}$	$10.18^{+8.79}_{-8.87}$	$1.75^{+0.03}_{-0.03}$	0.71 ± 1.20	$8.61^{+8.87}_{-8.85}$	$11.77^{+12.15}_{-12.03}$
MACS1206.2-0847	27	181.5469134	-8.7954315	256.33	0.24	1.06	$13.12^{+9.55}_{-3.38}$	$10.49^{+10.24}_{-9.93}$	$1.20^{+0.77}_{-0.16}$	1.04 ± 0.40	$8.27^{+7.82}_{-7.87}$	$11.29^{+11.17}_{-10.96}$
MACS1206.2-0847	54	181.5664156	-8.7998352	51.01	0.04	2.06	$0.01^{+0.00}_{-0.00}$	$10.28^{+9.03}_{-9.18}$	$1.60^{+0.10}_{-0.08}$	1.13 ± 0.45	$8.31^{+7.96}_{-7.91}$	$11.71^{+11.60}_{-11.39}$
MACS1206.2-0847	55	181.5447563	-8.8001610	239.20	0.66	1.02	$8.78^{+3.02}_{-2.95}$	$10.29^{+9.01}_{-9.11}$	$1.34^{+0.07}_{-0.08}$	1.15 ± 0.28	$8.19^{+7.65}_{-7.59}$	$11.21^{+11.04}_{-10.83}$
MACS1206.2-0847	58	181.5506090	-8.8009850	762.01	0.11	0.56	$0.67^{+0.57}_{-0.49}$	$9.65^{+8.94}_{-8.54}$	$1.26^{+0.37}_{-0.34}$	0.52	$6.85^{+6.05}_{-6.00}$	$9.67^{+9.48}_{-9.24}$
MACS1206.2-0847	60	181.5447729	-8.8014626	233.13	1.06	-1.00	$0.00^{+0.00}_{-0.00}$	...	$0.00^{+0.00}_{-0.00}$	1.28 ± 0.35	...	...

Table 4.1: Properties of ALMA sources and corresponding optical counterparts.

cluster	ID	RA	DEC	SNR_{F160W}	sep [arcsecond]	z_{phot}	SFR_{EAZY} $[\log(M_\odot/yr^{-1})]$	$M_\star$ $[\log(M_\odot)]$	A_V [mag]	$S_{1.2mm}$ [mJy]	M_{dust} $[\log(M_\odot)]$	L_{IR} $[\log(L_\odot)]$
MACS1206.2-0847	61	181.5449871	-8.8024698	408.18	1.03	0.57	$0.01^{+0.00}_{-0.00}$	$9.96^{+8.48}_{-8.43}$	$0.91^{+0.07}_{-0.07}$	1.50 ± 0.40	$8.28^{+7.77}_{-7.74}$	$10.15^{+9.68}_{-9.63}$
MACS1206.2-0847	38	181.5343916	-8.7975222	189.69	0.04	1.15	$14.69^{+3.97}_{-5.55}$	$10.38^{+9.94}_{-9.32}$	$2.44^{+0.15}_{-0.30}$	0.27	$7.77^{+6.78}_{-6.82}$	$9.79^{+9.13}_{-8.96}$
MACS1206.2-0847	84	181.5547108	-8.8075633	407.82	0.48	0.51	$8.46^{+10.01}_{--3.67}$	$10.51_{-10.19}$	$1.28^{+-0.01}_{-0.52}$	0.43 ± 0.49	$8.04^{+8.11}_{-8.09}$	$9.87^{+10.00}_{-9.93}$
MACS1311.0-0310	27	197.7554922	-3.1759898	262.03	0.27	2.42	$20.73^{+0.70}_{-1.07}$	$10.17^{+8.83}_{-8.82}$	$0.79^{+0.03}_{-0.04}$	1.15 ± 0.49	$7.76^{+7.39}_{-7.41}$	$11.28^{+11.16}_{-10.96}$
MACS1311.0-0310	33	197.7505853	-3.1784355	27.60	0.08	1.81	$0.60^{+0.41}_{-0.32}$	$10.49^{+9.64}_{-9.57}$	$2.63^{+0.05}_{-0.04}$	0.67	$8.38^{+7.50}_{-7.40}$	$11.70^{+11.44}_{-11.26}$
MACS1423.8+2404	38	215.9458700	24.0817102	139.24	0.17	1.95	$8.10^{+12.11}_{-8.06}$	$10.38^{+10.24}_{-9.36}$	$2.13^{+0.45}_{-0.65}$	0.64 ± 0.65	$8.04^{+8.03}_{-8.06}$	$11.38^{+11.51}_{-11.39}$
MACS1423.8+2404	50	215.9494919	24.0784418	644.11	0.10	0.81	$534.63^{+160.44}_{-153.85}$	$11.82^{+10.23}_{-10.68}$	$1.32^{+0.04}_{-0.07}$	1.81	$9.49^{+8.66}_{-8.56}$	$12.43^{+12.21}_{-11.99}$
MACS1423.8+2404	52	215.9481902	24.0771052	135.82	0.31	0.97	$2.59^{+0.39}_{-0.16}$	$9.63^{+8.11}_{-8.85}$	$2.20^{+0.22}_{-0.16}$	0.17	$7.48^{+6.56}_{-6.54}$	$10.48^{+10.31}_{-10.05}$
MACS1423.8+2404	76	215.9501077	24.0700621	101.56	0.69	4.33	$128.18^{+1.26}_{-1.73}$	$10.57^{+8.35}_{-8.48}$	$0.77^{+0.00}_{-0.01}$	0.46 ± 0.57	$7.37^{+7.49}_{-7.48}$	$11.45^{+11.62}_{-11.57}$
MACS1931.8-2635	41	292.9568020	-26.5758904	972.76	0.08	0.32	$65.56^{+2.45}_{-2.61}$	$10.33^{+8.79}_{-8.75}$	$1.27^{+0.08}_{-0.10}$	5.65 ± 0.08	$9.40^{+8.68}_{-8.59}$	$12.12^{+11.93}_{-11.72}$
MACS1931.8-2635	47	292.9669811	-26.5767779	13.60	0.19	1.79	$0.00^{+0.00}_{-0.00}$	$9.75^{+8.87}_{-9.14}$	$1.94^{+0.04}_{-0.37}$	0.65	$8.50^{+7.62}_{-7.53}$	$11.82^{+11.56}_{-11.38}$
MACS1931.8-2635	55	292.9504041	-26.5787259	20.11	0.56	3.59	$35.25^{+2.04}_{-2.25}$	$10.76^{+9.72}_{-9.88}$	$1.97^{+0.05}_{-0.07}$	1.34 ± 0.46	$8.22^{+7.86}_{-7.77}$	$12.11^{+11.93}_{-11.73}$
MACS1931.8-2635	61	292.9553168	-26.5808187	35.00	0.65	4.17	$42.71^{+1.93}_{-7.54}$	$10.11^{+8.68}_{-8.08}$	$0.78^{+0.01}_{-0.06}$	1.18 ± 0.46	$8.17^{+7.84}_{-7.77}$	$12.22^{+12.05}_{-11.89}$
MACS1931.8-2635	42	292.9561655	-26.5753642	163.59	0.25	0.32	$0.60^{+0.00}_{-0.00}$	$8.26^{+6.57}_{-6.62}$	$1.05^{+0.04}_{-0.05}$	5.37	$9.38^{+8.68}_{-8.54}$	$12.10^{+11.93}_{-11.71}$
MACS1931.8-2635	69	292.9484625	-26.5839529	13.65	0.11	3.23	$17.23^{+2.54}_{-2.45}$	$10.21^{+9.42}_{-9.22}$	$1.21^{+0.11}_{-0.08}$	0.16	$7.57^{+6.76}_{-6.75}$	$11.35^{+11.08}_{-10.84}$
MACS2129.4-0741	24	322.3553503	-7.6854665	8.34	2.19	0.99	$0.00^{+0.00}_{-0.00}$	$8.16^{+7.38}_{-7.28}$	$0.90^{+0.10}_{-0.11}$	0.50 ± 0.63	$8.36^{+8.44}_{-8.47}$	$11.31^{+11.55}_{-11.45}$
MACS2129.4-0741	46	322.3727048	-7.6919880	82.22	0.14	1.47	$7.42^{+2.23}_{-0.66}$	$10.11^{+9.60}_{-9.51}$	$2.08^{+0.46}_{-0.07}$	0.35 ± 0.33	$7.93^{+7.94}_{-7.90}$	$11.11^{+11.24}_{-11.08}$
MACS2129.4-0741	62	322.3734434	-7.6937960	109.99	0.11	1.45	$11.81^{+5.80}_{-3.74}$	$10.35^{+9.36}_{-8.93}$	$2.45^{+0.18}_{-0.17}$	0.32 ± 0.74	$8.04^{+8.39}_{-8.40}$	$11.21^{+11.63}_{-11.58}$
PLCKG171.9-40.7	69	48.2198449	8.3791528	...	1.91	3.18	$7.26^{+0.52}_{-2.45}$	$10.11^{+9.11}_{-9.12}$	$0.34^{+0.24}_{-0.24}$	1.69 ± 0.22	$8.49^{+7.83}_{-7.77}$	$12.27^{+11.97}_{-11.80}$
PLCKG171.9-40.7	162	48.2446035	8.3914414	...	2.72	0.36	$0.01^{+0.00}_{-0.00}$	$9.31_{--6.15}$	$0.11^{+0.00}_{-0.00}$	-2.69	...	...

Table 4.1: Properties of ALMA sources and corresponding optical counterparts.

cluster	ID	RA	DEC	SNR_{F160W}	sep [arcsecond]	z_{phot}	SFR_{EAZY} $[\log(M_\odot/yr^{-1})]$	$M_\star$ $[\log(M_\odot)]$	A_V [mag]	$S_{1.2mm}$ [mJy]	M_{dust} $[\log(M_\odot)]$	L_{IR} $[\log(L_\odot)]$
PLCKG171.9-40.7	177	48.2311509	8.3955503	...	0.17	0.69	$3.11^{+-0.14}_{-2.18}$	$10.79^{+10.51}_{-10.51}$	$2.68^{+0.09}_{-1.99}$	1.31 ± 0.46	$8.46^{+8.03}_{-8.00}$	$10.35^{+9.96}_{-9.93}$
PLCKG171.9-40.7	161	48.2306214	8.3954731	...	0.67	1.46	$37.04^{+23.13}_{-14.98}$	$12.44^{+12.07}_{-12.26}$	$2.83^{+0.03}_{-0.18}$	2.21 ± 0.28	$8.87^{+8.12}_{-8.04}$	$10.98^{+10.36}_{-10.29}$
RXCJ0032.1+1808	32	8.0406932	18.1067957	...	0.16	3.56	$20.06^{+0.01}_{-0.02}$	$10.21^{+9.13}_{-9.00}$	$0.78^{+0.07}_{-0.05}$	0.75	$7.87^{+7.16}_{-7.03}$	$11.77^{+11.41}_{-11.28}$
RXCJ0032.1+1808	53	8.0342690	18.1112068	0.00	0.32	4.34	$16.44^{+2.62}_{-6.61}$	$10.06^{+9.79}_{-9.31}$	$2.23^{+0.13}_{-0.47}$	1.61 ± 0.26	$7.73^{+7.18}_{-7.09}$	$11.82^{+11.54}_{-11.31}$
RXCJ0032.1+1808	55	8.0326614	18.1128138	63.62	0.20	3.81	$2.55^{+0.60}_{-0.56}$	$10.13^{+8.98}_{-8.96}$	$0.93^{+0.09}_{-0.11}$	3.11 ± 0.25	$7.74^{+7.08}_{-7.01}$	$11.70^{+11.39}_{-11.22}$
RXCJ0032.1+1808	57	8.0321383	18.1135584	65.96	0.49	0.57	$0.00^{+0.00}_{-0.00}$	$8.80^{+7.58}_{-7.48}$	$0.48^{+0.06}_{-0.08}$	-1.31	...	...
RXCJ0032.1+1808	58	8.0315196	18.1142688	72.45	0.12	3.80	$9.34^{+8.00}_{-6.36}$	$10.09^{+9.25}_{-9.36}$	$0.66^{+0.09}_{-0.09}$	1.54 ± 0.33	$8.31^{+7.76}_{-7.71}$	$10.95^{+10.40}_{-10.33}$
RXCJ0032.1+1808	81	8.0535714	18.1172188	45.51	0.35	1.91	$8.22^{+0.48}_{-0.69}$	$9.58^{+8.34}_{-8.35}$	$0.82^{+0.03}_{-0.04}$	0.55	$7.99^{+7.10}_{-7.01}$	$10.22^{+9.48}_{-9.43}$
RXCJ0032.1+1808	127	8.0548414	18.1372963	11.44	0.55	2.73	$1.94^{+0.12}_{-0.14}$	$10.02^{+8.94}_{-9.12}$	$2.39^{+0.04}_{-0.06}$	4.25 ± 0.14	$8.70^{+7.88}_{-7.78}$	$11.12^{+10.38}_{-10.34}$
RXCJ0032.1+1808	131	8.0507777	18.1370193	5.84	0.23	2.54	$1.46^{+1.31}_{-1.36}$	$10.94^{+10.15}_{-10.17}$	$1.97^{+0.21}_{-0.25}$	4.21 ± 0.17	$9.06^{+8.22}_{-8.12}$	$11.44^{+10.69}_{-10.64}$
RXCJ0032.1+1808	198	8.0355827	18.1407431	8.55	0.41	3.43	$36.65^{+4.67}_{-21.11}$	$10.67^{+9.85}_{-9.97}$	$1.77^{+0.06}_{-0.32}$	1.35	$8.77^{+7.91}_{-7.83}$	$11.36^{+10.56}_{-10.49}$
RXCJ0032.1+1808	208	8.0582100	18.1426942	3.83	0.13	3.71	$6.17^{+8.26}_{-6.14}$	$9.90^{+9.62}_{-9.41}$	$1.83^{+0.44}_{-0.45}$	1.42	$8.50^{+7.75}_{-7.55}$	$11.13^{+10.31}_{-10.36}$
RXCJ0032.1+1808	220	8.0358851	18.1524648	...	0.79	1.53	$0.87^{+0.27}_{-0.37}$	$10.65^{+10.14}$	$0.41^{+0.42}_{--0.03}$	0.91 ± 0.58	$8.54^{+8.36}_{-8.35}$	$10.67^{+10.54}_{-10.49}$
RXCJ0032.1+1808	276	8.0358657	18.1497658	12.37	2.14	3.07	$1.05^{+2.39}_{-0.09}$	$9.36^{+6.17}_{-8.92}$	$0.09^{+0.18}_{-0.03}$	1.07	$8.59^{+7.74}_{-7.65}$	$11.09^{+10.32}_{-10.26}$
RXCJ0032.1+1808	287	8.0320960	18.1480371	11.99	0.14	2.70	$0.07^{+0.01}_{-0.01}$	$10.65^{+9.92}_{-9.93}$	$0.84^{+0.35}_{-0.33}$	0.98	$8.76^{+7.92}_{-7.79}$	$11.18^{+10.40}_{-10.38}$
RXCJ0032.1+1808	304	8.0373105	18.1449397	2.97	0.30	2.20	$0.01^{+0.00}_{-0.00}$	$9.87^{+8.58}_{-9.42}$	$1.59^{+0.06}_{-0.51}$	1.03 ± 0.25	$8.63^{+8.06}_{-8.03}$	$10.92^{+10.41}_{-10.35}$
RXCJ0032.1+1808	63	8.0474404	18.1145036	38.03	0.64	0.32	$0.02^{+0.03}_{-0.02}$	$7.99^{+6.66}_{-7.14}$	$1.14^{+0.09}_{-0.17}$	0.47	$7.79^{+6.82}_{-6.76}$	$9.58^{+8.91}_{-8.83}$
RXCJ0032.1+1808	162	8.0480361	18.1311965	1041.36	0.15	0.41	$5.09^{+3.48}_{-4.50}$	$11.28^{+10.40}_{-10.43}$	$0.79^{+0.12}_{-0.11}$	0.44	$7.92^{+6.95}_{-6.86}$	$9.74^{+9.03}_{-8.99}$
RXCJ0032.1+1808	245	8.0394333	18.1580407	...	2.29	0.10	$0.00^{+0.00}_{-0.00}$	$6.03^{+5.98}_{-5.56}$	$0.39^{+0.53}_{-0.32}$	0.46 ± 0.58	$6.87^{+6.97}_{-6.97}$	$8.57^{+8.71}_{-8.67}$
RXCJ0600.1-2007	67	90.0208748	-20.1567574	...	2.57	0.37	$0.17^{+0.55}_{-0.14}$	$10.32^{+8.44}_{-9.72}$	$0.48^{+0.23}_{-0.12}$	2.37 ± 0.13	$9.11^{+8.38}_{-8.29}$	$11.85^{+11.65}_{-11.45}$

Table 4.1: Properties of ALMA sources and corresponding optical counterparts.

cluster	ID	RA	DEC	SNR_{F160W}	sep [arcsecond]	z_{phot}	SFR_{EAZY} $[\log(M_\odot/yr^{-1})]$	$M_\star$ $[\log(M_\odot)]$	A_V [mag]	$S_{1.2mm}$ [mJy]	M_{dust} $[\log(M_\odot)]$	L_{IR} $[\log(L_\odot)]$
RXCJ0600.1-2007	111	90.0371425	-20.1488705	167.22	0.30	1.56	$0.08^{+0.01}_{-0.02}$	$11.22^{+9.80}_{-10.09}$	$1.31^{+0.07}_{-0.10}$	0.54	$8.17^{+7.27}_{-7.18}$	$11.40^{+11.18}_{-10.96}$
RXCJ0600.1-2007	164	90.0379199	-20.1407069	25.86	0.58	4.38	$43.93^{+1.97}_{-1.52}$	$10.18^{+8.54}_{-8.43}$	$0.56^{+0.03}_{-0.02}$	0.76 ± 0.68	$7.82^{+7.81}_{-7.78}$	$11.91^{+12.02}_{-11.86}$
RXCJ0949.8+1707	10	147.4672003	17.0964321	...	2.45	1.08	$2.19^{+0.16}_{-0.17}$	$9.15^{+7.94}_{-7.84}$	$1.07^{+0.05}_{-0.04}$	5.51 ± 0.06	$9.41^{+8.53}_{-8.42}$	$12.46^{+12.20}_{-12.02}$
RXCJ0949.8+1707	19	147.4743782	17.0993478	...	2.24	0.30	$0.00^{+0.00}_{-0.00}$	$9.70^{+7.57}_{-8.62}$	$0.12^{+0.00}_{-0.00}$	1.01 ± 0.32	$8.63^{+8.25}_{-8.17}$	$11.34^{+11.27}_{-11.04}$
RXCJ0949.8+1707	122	147.4631762	17.1368889	73.64	1.21	-1.00	$0.00^{+0.00}_{-0.00}$	...	$0.00^{+0.00}_{-0.00}$	0.61	...	...
RXCJ0949.8+1707	124	147.4775828	17.1362404	...	1.40	1.24	$2.86^{+1.93}_{-0.98}$	$9.97^{+9.00}_{-9.52}$	$0.44^{+0.35}_{-0.14}$	-2.19	...	...
RXCJ0949.8+1707	14	147.4681688	17.0962861	...	1.59	3.95	$7.88^{+3.10}_{-4.14}$	$11.27^{+10.62}_{-10.87}$	$2.64^{+0.06}_{-0.19}$	-0.73	...	...
RXCJ0949.8+1707	119	147.4671533	17.1360239	435.02	0.10	0.56	$18.61^{+4.54}_{-2.79}$	$10.64_{-10.47}$	$1.21^{+-0.03}_{-0.36}$	0.42 ± 0.49	$7.90^{+7.98}_{-8.00}$	$9.77^{+9.83}_{-9.86}$
RXJ1347-1145	41	206.8796443	-11.7441022	298.95	0.34	0.84	$4.87^{+2.96}_{--0.06}$	$10.16^{+7.46}_{-9.78}$	$0.98^{+0.18}_{-0.20}$	0.56 ± 0.31	$8.07^{+7.80}_{-7.82}$	$11.00^{+10.98}_{-10.78}$
RXJ1347-1145	51	206.8905708	-11.7469165	18.33	1.03	2.20	$0.42^{+0.04}_{-0.04}$	$8.14^{+7.33}_{-7.29}$	$0.07^{+0.00}_{-0.00}$	0.20	$7.36^{+6.49}_{-6.42}$	$10.83^{+10.54}_{-10.35}$
RXJ1347-1145	75	206.8776098	-11.7526462	780.57	0.11	0.64	$53.42^{+44.43}_{-42.14}$	$11.61^{+10.70}_{-10.65}$	$1.24^{+0.23}_{-0.25}$	3.06	$9.55^{+8.71}_{-8.66}$	$12.42^{+12.26}_{-12.01}$
RXJ1347-1145	145	206.8651991	-11.7641845	111.53	0.11	1.50	$35.01^{+1.33}_{-1.31}$	$10.65^{+9.52}_{-9.32}$	$1.85^{+0.04}_{-0.02}$	1.62 ± 0.29	$8.69^{+8.04}_{-7.96}$	$11.90^{+11.71}_{-11.47}$
RXJ1347-1145	148	206.8660282	-11.7654970	97.05	0.59	1.64	$22.90^{+0.80}_{-0.98}$	$10.74^{+9.50}_{-9.27}$	$2.15^{+0.03}_{-0.02}$	2.45 ± 0.13	$8.70^{+7.82}_{-7.76}$	$11.96^{+11.71}_{-11.52}$
RXJ1347-1145	166	206.8666684	-11.7700462	...	0.38	2.65	$0.18^{+0.27}_{-0.12}$	$11.33^{+10.76}_{-10.97}$	$0.12^{+0.01}_{-0.00}$	0.52	$7.95^{+7.19}_{-7.09}$	$11.56^{+11.30}_{-11.09}$
RXJ2129.7+0005	24	322.3553503	-7.6854665	8.34	2.19	0.99	$0.00^{+0.00}_{-0.00}$	$8.16^{+7.38}_{-7.28}$	$0.90^{+0.10}_{-0.11}$	0.50 ± 0.63	$8.36^{+8.44}_{-8.47}$	$11.31^{+11.55}_{-11.45}$
RXJ2129.7+0005	46	322.3727048	-7.6919880	82.22	0.14	1.47	$7.42^{+2.23}_{-0.66}$	$10.11^{+9.60}_{-9.51}$	$2.08^{+0.46}_{-0.07}$	0.35 ± 0.33	$7.93^{+7.94}_{-7.91}$	$11.11^{+11.22}_{-11.11}$
RXJ2129.7+0005	62	322.3734434	-7.6937960	109.99	0.11	1.45	$11.81^{+5.80}_{-3.74}$	$10.35^{+9.36}_{-8.93}$	$2.45^{+0.18}_{-0.17}$	0.32 ± 0.74	$8.07^{+8.37}_{-8.41}$	$11.20^{+11.66}_{-11.57}$
RXCJ2211.7-0350	19	332.9487419	-3.8509998	...	1.41	2.85	$7.01^{+1.39}_{-2.93}$	$11.46^{+9.27}_{-10.51}$	$0.45^{+0.28}_{-0.33}$	0.67 ± 0.41	$8.18^{+7.96}_{-7.97}$	$11.82^{+11.77}_{-11.63}$
RXCJ2211.7-0350	35	332.9287744	-3.8449034	...	0.89	1.89	$38.56^{+25.38}_{-33.20}$	$10.97_{-10.48}$	$1.85^{+0.00}_{-0.46}$	2.62 ± 0.26	$8.80^{+8.06}_{-7.97}$	$12.16^{+11.93}_{-11.73}$
RXCJ2211.7-0350	171	332.9258442	-3.8399459	65.76	0.34	1.75	$22.36^{+1.32}_{-0.96}$	$10.83^{+9.69}_{-9.65}$	$2.23^{+0.03}_{-0.04}$	1.14 ± 0.45	$8.61^{+8.24}_{-8.22}$	$11.90^{+11.77}_{-11.57}$

Table 4.1: Properties of ALMA sources and corresponding optical counterparts.

cluster	ID	RA	DEC	$\mathrm{SNR}_{\mathrm{F160W}}$	sep [arcsecond]	z_{phot}	$\mathrm{SFR}_{\mathrm{EAZY}}$ $[\log(M_\odot/\mathrm{yr}^{-1})]$	$M_\star$ $[\log(M_\odot)]$	A_V [mag]	$S_{1.2\mathrm{mm}}$ [mJy]	M_{dust} $[\log(M_\odot)]$	L_{IR} $[\log(L_\odot)]$
RXCJ2211.7-0350	164	332.9363309	-3.8371329	8.03	0.19	4.92	$44.61^{+34.67}_{-30.19}$	$10.60^{+10.38}_{-10.11}$	$0.78^{+0.42}_{-0.66}$	0.38	$7.66^{+7.06}_{-6.95}$	$11.91^{+11.59}_{-11.41}$
SMACSJ0723.3-7327	61	110.7660662	-73.4517267	35.50	0.25	2.12	$0.03^{+0.01}_{-0.01}$	$11.04_{-10.32}$	$1.60^{+0.13}_{-0.36}$	0.80 ± 0.34	$8.30^{+7.93}_{-7.95}$	$11.72^{+11.61}_{-11.40}$
SMACSJ0723.3-7327	93	110.7631337	-73.4558425	104.23	0.65	0.46	$0.00^{+0.00}_{-0.00}$	$9.27^{+8.30}_{-8.16}$	$0.14^{+0.04}_{-0.03}$	0.87 ± 0.42	$8.76^{+8.52}_{-8.45}$	$11.53^{+11.50}_{-11.30}$
SMACSJ0723.3-7327	124	110.8545175	-73.4608018	90.79	0.74	1.05	$4.04^{+1.26}_{-1.03}$	$9.81^{+8.55}_{-8.58}$	$1.19^{+0.06}_{-0.06}$	0.44	$8.27^{+7.37}_{-7.32}$	$11.30^{+11.12}_{-10.88}$
SMACSJ0723.3-7327	98	110.7609477	-73.4569162	99.52	0.63	2.01	$0.41^{+0.29}_{-0.38}$	$10.31_{-9.72}$	$0.12^{+0.00}_{-0.01}$	0.45	$8.09^{+7.23}_{-7.11}$	$11.49^{+11.23}_{-11.03}$

5 Perspectives

In this thesis, we primitively want to focus on the study of dusty galaxies, yet not all of our sources turn out to be one of them. To confirm which are really dusty galaxies, the cross-check of SEDs and the UVJ diagram can be carried out. Also, as mentioned in previous sections, H-dropout, even infrared-dropout ALMA-detected sources will be of large interest because they are potential extremely dusty galaxies.

Besides, given the potential coupling between $L_{\rm IR}$ and $M_{\rm dust}$, it is hard to measure SFE$\equiv$ SFR$/M_{\rm gas}$ by assuming $M_{\rm gas}/M_{\rm dust}$. Thus, we hope that cooling line maps, i.e. [CII] 158μm or molecular lines, i.e. low-J CO lines, can be used for calculating $M_{\rm gas}$ independently and comparing with SFR$_{\rm IR}$ and $M_{\rm dust}$.

6 Conclusion

In this thesis, we have presented spatially matched results of UV/optical counterparts of ALCS-detected sources and studied their properties. Our major results are as follows:

- For our samples, the UVJ diagram can distinguish quiescent galaxies and star-forming galaxies with an accuracy of $\sim 90\%$. Most ALMA-detected objects have UV/optical counterparts in the main sequence, according to UVJ diagrams.

- For our dusty star-forming galaxies, we use infrared luminosity deduced from rescaled SEDs based on ALMA 1.2 mm flux density and UV luminosity based on NUV flux from UV/optical SED fitting to compute $\mathrm{SFR_{UV+IR}}$. We find that indicators based on UV and infrared luminosity can better describe SFRs of them which generally fall in the main sequence, while SFRs deduced from EAZY are likely underestimated, due to the limits of models.

- We use flux density at Rayleigh-Jeans tail of rescaled SEDs to deduce M_{dust} of galaxies. For our dusty star-forming galaxies at $z > 0.5$, the IRX-$M_\star$ agrees with the relationship from Bouwens *et al.*, 2016 well, which has the form of $\log_{10}(\mathrm{IRX}) \propto \log_{10}(M_\star)$.

- For our dusty star-forming galaxies at $z > 0.5$, the slope of $M_{\mathrm{dust}}/M_\star$ is consistent with the result from Magdis *et al.*, 2012, which has the form of $M_{\mathrm{dust}}/M_\star \propto M_\star^{-0.5}$. The outliers under the main sequence at high redshift are likely due to our strategies of modified black body. The median values of $M_{\mathrm{dust}}/M_\star$ agree with mean ratios of $M_{dust}/M_\star$ for main sequence galaxies from Béthermin *et al.*, 2015, ranging from $0.001 \sim 0.01$.

- For our dusty star-forming galaxies, the cluster lensing can magnify the flux by a factor of $3 \sim 5$ in average, meaning that the time of exposure is

reduced to $1/25 \sim 1/9$ of the time needed without lensing. Thus cluster lensing is a powerful and efficient tool for us to probe the faintest galaxies in the universe.

Due to the selection effect of choosing ALMA sources with optical counterparts, our samples are probing normal star-forming galaxies with a moderate amount of dust. To improve the completeness of dusty candidates, selection based on photometry at longer wavelengths is needed.

Bibliography

Abramson, Louis E., Daniel D. Kelson, Alan Dressler, Bianca Poggianti, Michael D. Gladders, Jr. Oemler Augustus, and Benedetta Vulcani (Apr. 2014). „The Mass-independence of Specific Star Formation Rates in Galactic Disks“. In: *ApJ* 785.2, L36, p. L36. arXiv: 1402.7076 [astro-ph.GA].

Balogh, Michael L. and Simon L. Morris (Nov. 2000). „Hα photometry of Abell 2390“. In: *MNRAS* 318.3, pp. 703–714. arXiv: astro-ph/0007111 [astro-ph].

Bertin, E. and S. Arnouts (June 1996). „SExtractor: Software for source extraction.“ In: *A&AS* 117, pp. 393–404.

Béthermin, Matthieu, Emanuele Daddi, Georgios Magdis, *et al.* (Jan. 2015). „Evolution of the dust emission of massive galaxies up to z = 4 and constraints on their dominant mode of star formation“. In: *A&A* 573, A113, A113. arXiv: 1409.5796 [astro-ph.GA].

Bouwens, Rychard J., Manuel Aravena, Roberto Decarli, *et al.* (Dec. 2016). „ALMA Spectroscopic Survey in the Hubble Ultra Deep Field: The Infrared Excess of UV-Selected z = 2-10 Galaxies as a Function of UV-Continuum Slope and Stellar Mass“. In: *ApJ* 833.1, 72, p. 72. arXiv: 1606.05280 [astro-ph.GA].

Brammer, Gabe (May 2019). *Grizli: Grism redshift and line analysis software*. Astrophysics Source Code Library, record ascl:1905.001. ascl: 1905.001.

Brammer, Gabriel B., Pieter G. van Dokkum, and Paolo Coppi (Oct. 2008). „EAZY: A Fast, Public Photometric Redshift Code“. In: *ApJ* 686.2, pp. 1503–1513. arXiv: 0807.1533 [astro-ph].

Carnall, A. C., R. J. McLure, J. S. Dunlop, and R. Davé (Apr. 2021). *Bagpipes: Bayesian Analysis of Galaxies for Physical Inference and Parameter EStimation*. Astrophysics Source Code Library, record ascl:2104.017. ascl: 2104.017.

Casey, Caitlin M., Desika Narayanan, and Asantha Cooray (Aug. 2014). „Dusty star-forming galaxies at high redshift“. In: *Phys. Rep.* 541.2, pp. 45–161. arXiv: 1402.1456 [astro-ph.CO].

Chabrier, Gilles (July 2003). „Galactic Stellar and Substellar Initial Mass Function“. In: *PASP* 115.809, pp. 763–795. arXiv: astro-ph/0304382 [astro-ph].

Charnley, SB, AGGM Tielens, and TJ Millar (1992). „On the molecular complexity of the hot cores in Orion A-Grain surface chemistry as' The last refuge of the scoundrel“. In: *The Astrophysical Journal* 399, pp. L71–L74.

Coe, Dan, Brett Salmon, Maruša Bradač, *et al.* (Oct. 2019). „RELICS: Reionization Lensing Cluster Survey“. In: *ApJ* 884.1, 85, p. 85. arXiv: 1903.02002 [astro-ph.GA].

Daddi, E., M. Dickinson, G. Morrison, *et al.* (Nov. 2007). „Multiwavelength Study of Massive Galaxies at z~2. I. Star Formation and Galaxy Growth“. In: *ApJ* 670.1, pp. 156–172. arXiv: 0705.2831 [astro-ph].

Donevski, D., A. Lapi, K. Małek, *et al.* (Dec. 2020). „In pursuit of giants. I. The evolution of the dust-to-stellar mass ratio in distant dusty galaxies“. In: *A&A* 644, A144, A144. arXiv: 2008.09995 [astro-ph.GA].

Draine, B. T. and Aigen Li (Mar. 2007). „Infrared Emission from Interstellar Dust. IV. The Silicate-Graphite-PAH Model in the Post-Spitzer Era“. In: *ApJ* 657.2, pp. 810–837. arXiv: astro-ph/0608003 [astro-ph].

Dye, S., S. A. Eales, I. Aretxaga, *et al.* (May 2008). „The SCUBA HAlf Degree Extragalactic Survey (SHADES) - VII. Optical/IR photometry and stellar masses of submillimetre galaxies“. In: *MNRAS* 386.2, pp. 1107–1130. arXiv: 0802.0497 [astro-ph].

Gunn, James E. and III Gott J. Richard (Aug. 1972). „On the Infall of Matter Into Clusters of Galaxies and Some Effects on Their Evolution“. In: *ApJ* 176, p. 1.

Hausman, M. A. and J. P. Ostriker (Sept. 1978). „Galactic cannibalism. III. The morphological evolution of galaxies and clusters.“ In: *ApJ* 224, pp. 320–336.

Hennebelle, Patrick and Gilles Chabrier (Sept. 2008). „Analytical Theory for the Initial Mass Function: CO Clumps and Prestellar Cores“. In: *ApJ* 684.1, pp. 395–410. arXiv: 0805.0691 [astro-ph].

Howell, Steve B. (2006). *Handbook of CCD Astronomy*. 2nd ed. Cambridge Observing Handbooks for Research Astronomers. Cambridge University Press.

Johnson, H. L. and W. W. Morgan (May 1953). „Fundamental stellar photometry for standards of spectral type on the Revised System of the Yerkes Spectral Atlas.“ In: *ApJ* 117, p. 313.

Kennicutt, Robert C. and Neal J. Evans (Sept. 2012). „Star Formation in the Milky Way and Nearby Galaxies“. In: *ARA&A* 50, pp. 531–608. arXiv: 1204.3552 [astro-ph.GA].

Kohno, Kotaro (Dec. 2019). *The ALMA lensing cluster survey: initial outcomes.*

Kroupa, Pavel (Apr. 2001). „On the variation of the initial mass function“. In: *MNRAS* 322.2, pp. 231–246. arXiv: astro-ph/0009005 [astro-ph].

Krumholz, Mark R., Avishai Dekel, and Christopher F. McKee (Jan. 2012). „A Universal, Local Star Formation Law in Galactic Clouds, nearby Galaxies, High-redshift Disks, and Starbursts“. In: *ApJ* 745.1, 69, p. 69. arXiv: 1109.4150 [astro-ph.CO].

Lee, Nicholas, D. B. Sanders, Caitlin M. Casey, *et al.* (Mar. 2015). „A Turnover in the Galaxy Main Sequence of Star Formation at M $_*$ ~10^{10} M $_\odot$ for Redshifts z $<$ 1.3“. In: *ApJ* 801.2, 80, p. 80. arXiv: 1501.01080 [astro-ph.GA].

Li, Aigen and B. T. Draine (June 2001). „Infrared Emission from Interstellar Dust. II. The Diffuse Interstellar Medium“. In: *ApJ* 554.2, pp. 778–802. arXiv: astro-ph/0011319 [astro-ph].

Lotz, J. M., A. Koekemoer, D. Coe, *et al.* (Mar. 2017). „The Frontier Fields: Survey Design and Initial Results“. In: *ApJ* 837.1, 97, p. 97. arXiv: 1605.06567 [astro-ph.GA].

Magdis, Georgios E., E. Daddi, M. Béthermin, *et al.* (Nov. 2012). „The Evolving Interstellar Medium of Star-forming Galaxies since z = 2 as Probed by Their Infrared Spectral Energy Distributions“. In: *ApJ* 760.1, 6, p. 6. arXiv: 1210.1035 [astro-ph.CO].

Moffat, A. F. J. (Dec. 1969). „A Theoretical Investigation of Focal Stellar Images in the Photographic Emulsion and Application to Photographic Photometry“. In: *A&A* 3, p. 455.

Noeske, K. G., B. J. Weiner, S. M. Faber, *et al.* (May 2007). „Star Formation in AEGIS Field Galaxies since z=1.1: The Dominance of Gradually Declining Star Formation, and the Main Sequence of Star-forming Galaxies“. In: *ApJ* 660.1, pp. L43–L46. arXiv: astro-ph/0701924 [astro-ph].

Omukai, K., T. Tsuribe, R. Schneider, and A. Ferrara (June 2005). „Thermal and Fragmentation Properties of Star-forming Clouds in Low-Metallicity Environments“. In: *ApJ* 626.2, pp. 627–643. arXiv: astro-ph/0503010 [astro-ph].

Pearson, W. J., L. Wang, P. D. Hurley, K. Małek, V. Buat, D. Burgarella, D. Farrah, S. J. Oliver, D. J. B. Smith, and F. F. S. van der Tak (July 2018). „Main sequence of star forming galaxies beyond the Herschel confusion limit“. In: *A&A* 615, A146, A146. arXiv: 1804.03482 [astro-ph.GA].

Postman, Marc, Dan Coe, Narciso Benítez, *et al.* (Apr. 2012). „The Cluster Lensing and Supernova Survey with Hubble: An Overview“. In: *ApJS* 199.2, 25, p. 25. arXiv: 1106.3328 [astro-ph.CO].

Reddy, Naveen A., Charles C. Steidel, Dario Fadda, Lin Yan, Max Pettini, Alice E. Shapley, Dawn K. Erb, and Kurt L. Adelberger (June 2006). „Star Formation and Extinction in Redshift z~2 Galaxies: Inferences from Spitzer MIPS Observations“. In: *ApJ* 644.2, pp. 792–812. arXiv: astro-ph/0602596 [astro-ph].

Salpeter, Edwin E. (Jan. 1955). „The Luminosity Function and Stellar Evolution.“ In: *ApJ* 121, p. 161.

Schechter, P. (Jan. 1976). „An analytic expression for the luminosity function for galaxies.“ In: *ApJ* 203, pp. 297–306.

Schmidt, Maarten (Mar. 1959). „The Rate of Star Formation.“ In: *ApJ* 129, p. 243.

Schneider, R., A. Ferrara, and R. Salvaterra (July 2004). „Dust formation in very massive primordial supernovae“. In: *MNRAS* 351.4, pp. 1379–1386. arXiv: astro-ph/0307087 [astro-ph].

Schreiber, C., D. Elbaz, M. Pannella, L. Ciesla, T. Wang, and M. Franco (Jan. 2018). „Dust temperature and mid-to-total infrared color distributions for star-forming galaxies at $0 < z < 4$“. In: *A&A* 609, A30, A30. arXiv: 1710.10276 [astro-ph.GA].

Schreiber, C., M. Pannella, D. Elbaz, *et al.* (Mar. 2015). „The Herschel view of the dominant mode of galaxy growth from $z = 4$ to the present day“. In: *A&A* 575, A74, A74. arXiv: 1409.5433 [astro-ph.GA].

Siebenmorgen, R. and E. Krügel (Jan. 2007). „Dust in starburst nuclei and ULIRGs. SED models for observers“. In: *A&A* 461.2, pp. 445–453. arXiv: astro-ph/0606444 [astro-ph].

Silvia, Devin W., Britton D. Smith, and J. Michael Shull (June 2010). „Numerical Simulations of Supernova Dust Destruction. I. Cloud-crushing and Post-processed Grain Sputtering“. In: *ApJ* 715.2, pp. 1575–1590. arXiv: 1001.4793 [astro-ph.GA].

Speagle, J. S., C. L. Steinhardt, P. L. Capak, and J. D. Silverman (Oct. 2014). „A Highly Consistent Framework for the Evolution of the Star-Forming “Main Sequence” from z ~0-6“. In: *ApJS* 214.2, 15, p. 15. arXiv: 1405.2041 [astro-ph.GA].

Suess, Katherine A., Mariska Kriek, Sedona H. Price, and Guillermo Barro (July 2021). „Dissecting the Size-Mass and Σ_1-Mass Relations at $1.0 < z < 2.5$:

Galaxy Mass Profiles and Color Gradients as a Function of Spectral Shape“. In: *ApJ* 915.2, 87, p. 87. arXiv: 2101.05820 [astro-ph.GA].

Takeuchi, Tsutomu T., Fang-Ting Yuan, Akira Ikeyama, Katsuhiro L. Murata, and Akio K. Inoue (Aug. 2012). „Reexamination of the Infrared Excess-Ultraviolet Slope Relation of Local Galaxies“. In: *ApJ* 755.2, 144, p. 144. arXiv: 1206.3905 [astro-ph.CO].

Tremaine, S. D., J. P. Ostriker, and Jr. Spitzer L. (Mar. 1975). „The formation of the nuclei of galaxies. I. M31.“ In: *ApJ* 196, pp. 407–411.

van Albada, T. S. (Dec. 1982). „Dissipationless galaxy formation and the R to the 1/4-power law“. In: *MNRAS* 201, pp. 939–955.

Wang, L., F. Gao, P. N. Best, *et al.* (Apr. 2021). „The bright end of the infrared luminosity functions and the abundance of hyperluminous infrared galaxies“. In: *A&A* 648, A8, A8. arXiv: 2011.08798 [astro-ph.GA].

Whitaker, Katherine E., Marijn Franx, Joel Leja, *et al.* (Nov. 2014). „Constraining the Low-mass Slope of the Star Formation Sequence at $0.5 < z < 2.5$“. In: *ApJ* 795.2, 104, p. 104. arXiv: 1407.1843 [astro-ph.GA].

Whitaker, Katherine E., Ivo Labbé, Pieter G. van Dokkum, *et al.* (July 2011). „The NEWFIRM Medium-band Survey: Photometric Catalogs, Redshifts, and the Bimodal Color Distribution of Galaxies out to z ~3“. In: *ApJ* 735.2, 86, p. 86. arXiv: 1105.4609 [astro-ph.CO].

Whitaker, Katherine E., Pieter G. van Dokkum, Gabriel Brammer, and Marijn Franx (Aug. 2012). „The Star Formation Mass Sequence Out to $z = 2.5$“. In: *ApJ* 754.2, L29, p. L29. arXiv: 1205.0547 [astro-ph.CO].

Williams, Rik J., Ryan F. Quadri, Marijn Franx, Pieter van Dokkum, and Ivo Labbé (Feb. 2009). „Detection of Quiescent Galaxies in a Bicolor Sequence from Z = 0-2“. In: *ApJ* 691.2, pp. 1879–1895. arXiv: 0806.0625 [astro-ph].